POLITECNICO DI TORINO
Repository ISTITUZIONALE

A multi-technique approach to long-term structural health monitoring of the Garisenda Tower (Italy)

Original
A multi-technique approach to long-term structural health monitoring of the Garisenda Tower (Italy) / Lacidogna, G., Friedrich, L.F., Marin Montanari, P., Hamdan Padilha, M., Invernizzi, S., Di Tommaso, A., Iturrioz, I.. - In: STRUCTURAL HEALTH MONITORING. - ISSN 1475-9217. - STAMPA. - (2026), pp. 1-21. [10.1177/14759217261448084]

Availability:
This version is available at: 11583/3011407 since: 2026-05-26T14:27:25Z

Publisher:
SAGE Publications

Published
DOI:10.1177/14759217261448084

Terms of use:

This article is made available under terms and conditions as specified in the corresponding bibliographic description in the repository

Publisher copyright
Sage postprint/Author's Accepted Manuscript

(Article begins on next page)

19 October 2026

Version R1

April 2026

A MULTI-TECHNIQUE APPROACH TO LONG-TERM STRUCTURAL HEALTH MONITORING OF THE GARISENDA TOWER (ITALY)

Giuseppe Lacidogna[1*], Leandro Ferreira Friedrich[2], Pedro Marin Montanari[1], Mariana Hamdan Padilha[2], Stefano Invernizzi[1], Angelo Di Tommaso[3], and Ignacio Iturrioz[4]

[1]Department of Structural, Geotechnical and Building Engineering, Politecnico di Torino, 24, Corso Duca degli Abruzzi, 10129 Torino, Italy.

[2]Post-graduate Program in Engineering, Universidade Federal do Pampa, Av. Tiaraju 810, CEP 97546-550, Alegrete, Brazil.

[3]Former Professor Alma Mater Studiorum Università di Bologna, 40126 Bologna, Italy

[4]Mechanical Post-Graduate Program, Universidade Federal do Rio Grande do Sul, Sarmento Leite 425, CEP 90050-170, Porto Alegre, Brazil.

Corresponding author: giuseppe.lacidogna@polito.it

ABSTRACT

This study presents a comprehensive long-term structural health monitoring (SHM) approach for the Garisenda Tower in Bologna, Italy, combining multiple non-destructive techniques. Over a six-year period, data from Acoustic Emission (AE), Fiber Optic Sensors (FOS), and a pendulum system were integrated to assess the tower's micro- and macro-scale damage mechanisms, as well as global movements. Advanced statistical analyses—such as *b*-value, Hurst exponent, Natural Time, and Critical Fluctuation methods—were applied to AE time series, revealing damage evolution and shifts in structural behaviour around 2023. Results suggest that thermally induced stresses primarily drive damage progression initially, with microcracking strongly correlated to seasonal temperature variations. Post-2023, a transition toward autonomous damage processes was observed, indicating increased instability. The combined data confirm ongoing internal deterioration, emphasizing the importance of multi-technique, long-term monitoring for heritage preservation. Findings support proactive interventions to safeguard this iconic medieval structure against progressive instability.

KEYWORDS: Structural Health Monitoring, Acoustic Emission, Fiber Optic Sensors, Long-term Monitoring, Heritage Structures, Structural Damage, AE Time Series Analysis

1. INTRODUCTION

The Structural Health Monitoring (SHM) of historical towers requires balancing preservation with public safety, especially for tilted structures prone to progressive damage. While traditional methods focus on geometric displacements, emerging non-destructive techniques such as Acoustic Emission (AE) and Fiber Optic Sensors (FOS) offer valuable insights into micro-scale and global damage mechanisms.

This work is focused on the Garisenda Tower in Bologna, Italy. The tower, which represents one of the city's symbols and its valuable medieval heritage, was built in the early 12th century by the Garisendi family alongside the Asinelli Tower. Although the initial intentions of the builders were to reach a greater height, the Garisenda began to tilt in 1351 due to foundation failure, leading to a 13-meter reduction from its original 61 meters for safety reasons. Its stability has attracted scientific interest over time **[1-6]**. Currently, the towers are owned and maintained by the Municipality of Bologna.

Previous research on the tower has employed a comprehensive, multidisciplinary approach to assess its structural health and stability, integrating non-destructive testing, numerical modeling, and environmental monitoring techniques **[1,2,7,8]**. The tower's distinctive tilt and historical damage have prompted extensive monitoring using AE, FOS, seismometers, and laser surveys, which together provide insights into its ongoing structural evolution.

Overall, these integrated experimental and modelling efforts suggest that thermally induced stresses are important factors influencing damage progression in the Garisenda Tower, and that the ongoing application of advanced monitoring techniques—analysed with appropriate statistical methods—is essential for devising effective preservation strategies and ensuring long-term stability **[7-9]**.

This work continues with the aim of integrating multi-technique data over long-term periods, which are particularly suitable for heterogeneous medieval masonry subjected to combined thermal and seismic loads. Despite previous studies on the Garisenda Tower and similar heritage structures, most investigations have been limited to short-term monitoring campaigns or single-technique approaches. A clear gap remains in the literature regarding the availability of long-term, multi-scale datasets capable of capturing both micro- and macro-scale structural behaviour. The novelty of the present work lies in the combination of: (i) a six-year continuous monitoring dataset, which is rare for historical masonry structures; (ii) the integration of Acoustic Emission (AE), Fiber Optic Sensors (FOS), and pendulum measurements, enabling a multi-scale assessment of damage processes; and (iii) the application of advanced statistical tools to identify transitions in structural behaviour. This long-term, multi-technique integration fills a gap in the heritage SHM literature, where synergic micro- and macro-scale damage analyses are scarce. It should be clarified that the analyses presented in this paper are based on a selected subset of the data available

within the overall monitoring system, which comprises a broader and more complex dataset supporting predictive modelling activities that must be approached with the utmost caution.

2. OVERVIEW OF THE GARISENDA TOWER

The Torre della Garisenda, **Figure 1**, built in the early 12th century (between 1109 and 1119), belongs to the original group of approximately 90 medieval towers in Bologna, which served military and symbolic functions and were often associated with the prestige of noble families or political factions **[7,8,10]**. Currently, approximately twenty of these structures remain, notably the Asinelli and Garisenda towers, located at the entrance to the ancient Via Emilia, in the heart of the historic center **[10]**.

Figure 1. The Garisenda (left) and Asinelli (right) Towers in Bologna.

With a square base measuring approximately 7 meters per side, the tower was initially built 61 meters high, but was reduced by 13 meters in the 14th century due to a dangerous inclination detected at that time **[3,7,8,10]**. Its current inclination is approximately 4°, with a 3.22 m displacement at the top toward the southeast **[10]**, making it one of the steepest tilting towers in Europe, comparable to—and even superior to—the tilting Tower of Pisa in angular inclination **[11]**.

The structure is made of a "sacco" masonry, quite common in the construction of historic buildings and defensive structures of the period. This technique consists of two facings (a thicker inner and

a thinner outer) filled with stone and mortar **[3,7,8]**. Geophysical studies conducted between 1990 and 2000 by architect Francisco Giordano **[10]** revealed, through georadar analysis, that the first 80 cm of the base have superior characteristics to the rest of the masonry and that the foundation widens by approximately 1 m at a depth of approximately 2 m **[8]**.

Throughout history, the tower has undergone several transformations. Notable among these were the construction of wooden annexes in the 14th and 15th centuries, such as the "corridor," which connected the Garisenda to the Asinelli Tower at a height of approximately 30 m—a military structure built by order of Giovanni da Oleggio between 1355 and 1360. Subsequently, several buildings rested on the base of the tower (such as the chapel of the Madonna delle Grazie), all of which were removed by 1890, restoring its appearance free of annexes **[10]**.

Given its historical importance and delicate structural condition, the tower has been under monitoring for decades. Beginning in 2019, the City of Bologna—through its Department of Public Works—intensified this monitoring with the implementation of a continuous monitoring system, initially focused on measuring vertical deformations in the selenite base and thermal variables **[7]**. This system was progressively expanded with the integration of other advanced technologies, including acoustic emission sensors, optical strings, and a high-precision pendulum, which will be analyzed throughout this paper.

In October 2023, an increase in structural movement was identified, especially at the southwest base of the tower, leading the technical-scientific committee to recommend closing off the immediate area, blocking traffic and pedestrian access. A security perimeter was set up with containers and netting **[12]**.

In May 2025, the City Council announced the start of the structural restoration plan, with completion scheduled for 2028. The project involves techniques inspired by the stabilization of the Leaning Tower of Pisa, including the use of salvaged metal trusses, polyester retaining belts, and injections of special mortar underground to consolidate the foundations **[13]**.

3. MONITORING TECHNIQUES

In order to evaluate the stability of the Garisenda Tower and to understand the progression of its structural response over time, a multi-technique monitoring approach was implemented. The following sections describe the systems employed: acoustic emission sensors, which are responsible for detecting micro events associated with the formation and propagation of internal damage; optical strings, which are utilized to monitor strains along the tower's base; and a precision pendulum, which is employed to identify oscillations and global movements of the structure. Each technique is presented with its respective experimental configuration, operating principles, and type of data generated, with particular attention to the analysis and interpretation of the AE signals.

3.1 Acoustic Emission (AE)

AE is a non-destructive monitoring technique that facilitates real-time detection of internal degradation processes in materials and structures, including cracks, friction, or displacements at interfaces. These phenomena release elastic energy in the form of stress waves, which propagate through the structure and can be captured by piezoelectric (PZT) sensors installed on the surface of the sample or structure being monitored. Each acoustic emission event generates a short-duration transient signal, typically ranging in frequency from tens of kHz to several hundred kHz. The waveform and derived parameters (such as amplitude, energy, rise time, average frequency) of this signal provide information about the nature and severity of the generating source. The method is distinguished by its high sensitivity, enabling the detection of microdamage prior to its visibility, and its capacity to provide a dynamic and localized evaluation of structural activity **[9]**.

3.1.1 Experimental devices and test setup

The AE system installed at the base of the Garisenda Tower consists of two independent modules, designated AE001 and AE002, each equipped with eight acquisition channels connected to piezoelectric sensors. The initial module (AE001) was activated on 31st May 2019, while the subsequent module (AE002) became operational on 14th March 2023 **[14]**.

The piezoelectric sensor array utilized is the Lunitek AEmission LT18-003-PRD00-R0 model **[15]**, with a frequency response range

between 15 kHz and 625 kHz, rendering it suitable for the detection of acoustic emission events associated with the development of micro damage. These sensors were attached directly to the interior wall of the tower with a high-strength adhesive selected for its capacity to ensure reliable adhesion even under adverse environmental conditions.

The system operates at a sampling rate of 5 MS/s at 16 bits, thereby enabling high-resolution signal acquisition and real-time analysis. The subsequent processing of the captured waveforms is instrumental in the automatic extraction of pertinent parameters, including the amplitude, duration, energy, and average frequency. **Figure 2(a)** shows the sensor distribution scheme at the base of the tower, while **Figure 2(b)** shows the sensors installed in situ.

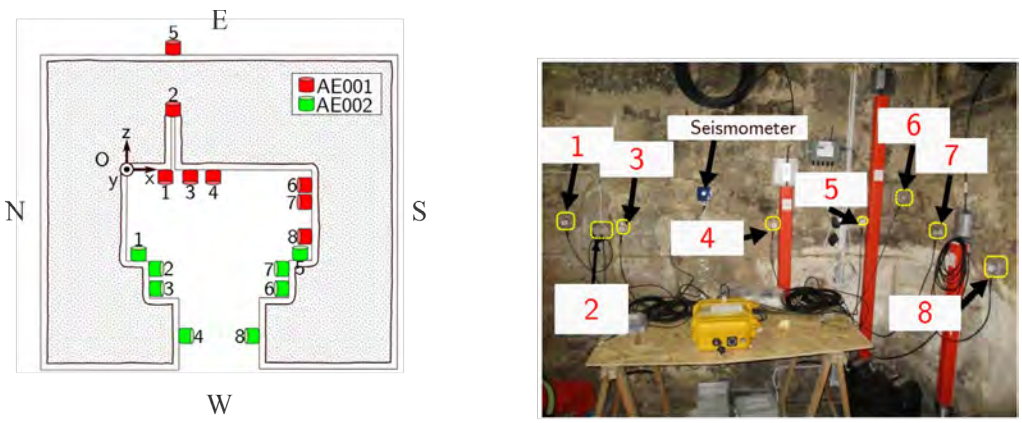

(a) (b)

Figure 2. (a) Layout illustrating the positioning of the PZT transducers around the base of the tower, (b) sensors of the system AE001 installed in the East wall of the tower base. Note that sensor 5 was initially installed inside the tower base, as shown

in (b), and was subsequently repositioned to the external location indicated in (a).

3.1.2 Identification of critical conditions by using AE time series

In order to assess the structural integrity of the tower and identify possible precursors of damage, a series of parameters were extracted from the AE time series. The parameters have been designed to capture different statistical, dynamical, and informational aspects of the signal, thus offering a multiscale view of the underlying physical processes. More precisely, the following indicators were considered:

- the b-value, derived from the Gutenberg–Richter relationship, commonly used to describe the amplitude distribution of AE events;
- the Hurst exponent, which quantifies the presence of long-term correlations or memory effects in the signal;
- the natural time analysis, a tool for detecting critical transitions in time series with irregular event occurrence;
- and the MCF-B approach, which is an approach employed in order to capture the crossover phenomenon, an indicator of critical condition;

In order to facilitate interpretation of these parameters and illustrate their diagnostic capability, a simplified and well-controlled experimental case is employed as a reference, see **Figure 3(a)**. In this example, the focus is on a concrete cube under uniaxial compression, where the transition from elastic behavior to structural failure was thoroughly observed through the use of AE

(the positions of the sensors are indicated in **Figure 3(a)**). The failure pattern of the sample is presented in **Figure 3(a)**, as well. In **Figure 3(b)**, the cumulative AE event count is presented alongside the normalized amplitude values (on the right-hand axis), together with the corresponding load evolution (out of scale). More details about the experimental setup, the loading conditions, and the devices used can be found in Ref. **[16]**. The same parameters listed above were employed during this AE test, enabling a direct association to be made between their temporal evolution and the mechanical degradation of the specimen. This reference scenario provides a foundation for comprehending the significance and critical thresholds of each indicator, thereby facilitating their application to a real-world case study of the Garisenda Tower.

(a) *b*-value

Definition: Studies in seismology and their connection to AE in engineering structures have significantly contributed to the theoretical understanding of how AE signals are related to damage processes in materials. A well-known example of this connection is the classic law proposed by Gutenberg and Richter **[17]**, which describes the statistical distribution of signal amplitudes through a universal exponential relationship. According to Shiotani et al. **[18]**, this is considered a universal law, meaning it is independent of the system's scale or the size of the structure. The law can be expressed as follows:

$$N(\geq A) = \zeta A^{-b} \quad \textbf{(1)}$$

where N is the cumulative number of events, A the signal amplitude, ζ is a constant and b is the b-value. More precisely, b represents the slope obtained from the linear fit between the signal amplitude and the cumulative number of events when both quantities are expressed on a logarithmic scale.

Interpretation: The evolution of the b-value throughout the compression test is shown in **Figure 3(c)**. The full duration of the test was segmented into 14 equal time intervals without overlapping, and the b-value was computed for each segment. For most of the loading phase (approximately 60% of the total test duration), the b-value remained relatively stable. However, a pronounced drop is observed in the final phase of the test, with the b-value decreasing from values above 1.5 to approximately 1. This behavior is significant: b-values approaching 1 are widely interpreted as indicators of critical damage evolution, where larger and more energetic acoustic emission events become dominant, signaling an imminent structural instability **[19]**.

(b) Hurst exponent

Definition: The influence of past events on critical events has been the subject of extensive research in a variety of complex systems **[20]**, through the analysis of characteristics associated with temporal persistence or long-term memory **[21]**. A well-established approach to quantifying the intensity of these correlations over

time is the so-called Hurst analysis **[22]**, also known as the rescaled interval (R^*/S^*) analysis.

The calculation of the Hurst exponent (H) is based on the statistical analysis of successive segments of the time series. For each window of size n, a cumulative profile $y(n)$ is constructed, from which the range R^* is determined. This is defined as the difference between the maximum and minimum values of the aforementioned profile, that is, $R^* = \max\,[y(n)] - \min\,[y(n)]$. This range is then normalized by the local variability of the segment, that is, divided by its standard deviation, S^*. This gives the R^*/S^* index for each window. By calculating the mean of the R^*/S^* values across all windows of a given size n, it can be observed that, for series with long-range correlation, this mean presents a power-type scaling relationship:

$$(R^* / S^*)_n \propto n^H \qquad \textbf{(2)}$$

Consequently, the exponent H corresponds to the slope derived from a least-squares regression performed on the log–log representation of R^*/S^* as a function of the window size n. Values of H >0.5 indicate persistence (future events tend to follow the same trend as previous ones), while H <0.5 suggests anti-persistence (a tendency to reverse). The case H =0.5 corresponds to a pure random process, with no memory.

Interpretation: **Figure 3(c)** shows the evolution of temporal correlations in AE amplitudes during compressive loading of the concrete cube. Up to 60% of the normalized time, the Hurst exponent stabilizes around 0.52, reflecting weak persistence. Thereafter, a progressive increase toward 0.6 is observed, aligned with the surge in event occurrence rate highlighted in **Figure 3(b)**. This correlation strengthening continues until peak stress conditions. Similar behaviors have been documented in seismic time series preceding major earthquakes **[23,24]**.

(c)Natural Time

Definition: Natural Time Analysis (NTA) was introduced in 2001 **[25]** as a novel statistical tool designed to distinguish low-frequency (≤ 1 Hz) seismic electric signals (SESs) from anthropogenic noise. Over time, NTA has proven effective in unveiling critical dynamics in seismic activity, contributing to improved accuracy in defining time windows for potential earthquake occurrences **[26,27]**. Unlike conventional continuous time representations, NTA employs a discrete-time framework, which allows it to uncover subtle dynamical patterns often hidden in complex systems. This characteristic makes it a valuable tool for identifying the progression toward critical states. A comprehensive overview of the method and its broad range of applications—including studies on AE time series—can be found in the review by Varotsos et al. **[28]**.

NT analysis examines the evolution of a system by focusing on the order of occurrence of events rather than on their conventional

temporal spacing **[25–28]**. For a sequence of N events, each event is represented by the normalized index $\chi_k = k/N$, which lies within the interval (0,1]. Instead of directly analyzing the raw amplitude, the method assigns to each event a quantity Q_k proportional to the released energy. The normalized weight of each event is expressed as $p_k = Q_k \Big/ \sum_{n=1}^{N} Q_n$. In AE applications, Q_k may correspond to either to the emitted AE energy or to the recorded signal amplitude **[29–31]**.

Thus, the statistical description of the sequence is based on the pair (χ_k, p_k), which incorporates both event ordering and energetic contribution.

The approach to criticality is evaluated through four complementary quantities derived from this representation: the variance κ_1, the entropy S, the entropy under time reversal S_{rev}, and the average distance $\langle D \rangle$.

The variance κ_1, **Eq.(3),** acts as an order parameter of the system, reflecting the internal organization of the sequence. Its convergence toward the theoretical critical value $\kappa_1 = 0.070$ indicates strengthening correlations among events.

$$\kappa_1 = \langle \chi^2 \rangle - \langle \chi \rangle^2 \equiv \sum_{k=1}^{N} p_k \left(\frac{k}{N} \right)^2 - \left(\sum_{k=1}^{N} \frac{k}{N} p_k \right)^2 \qquad \textbf{(3)}$$

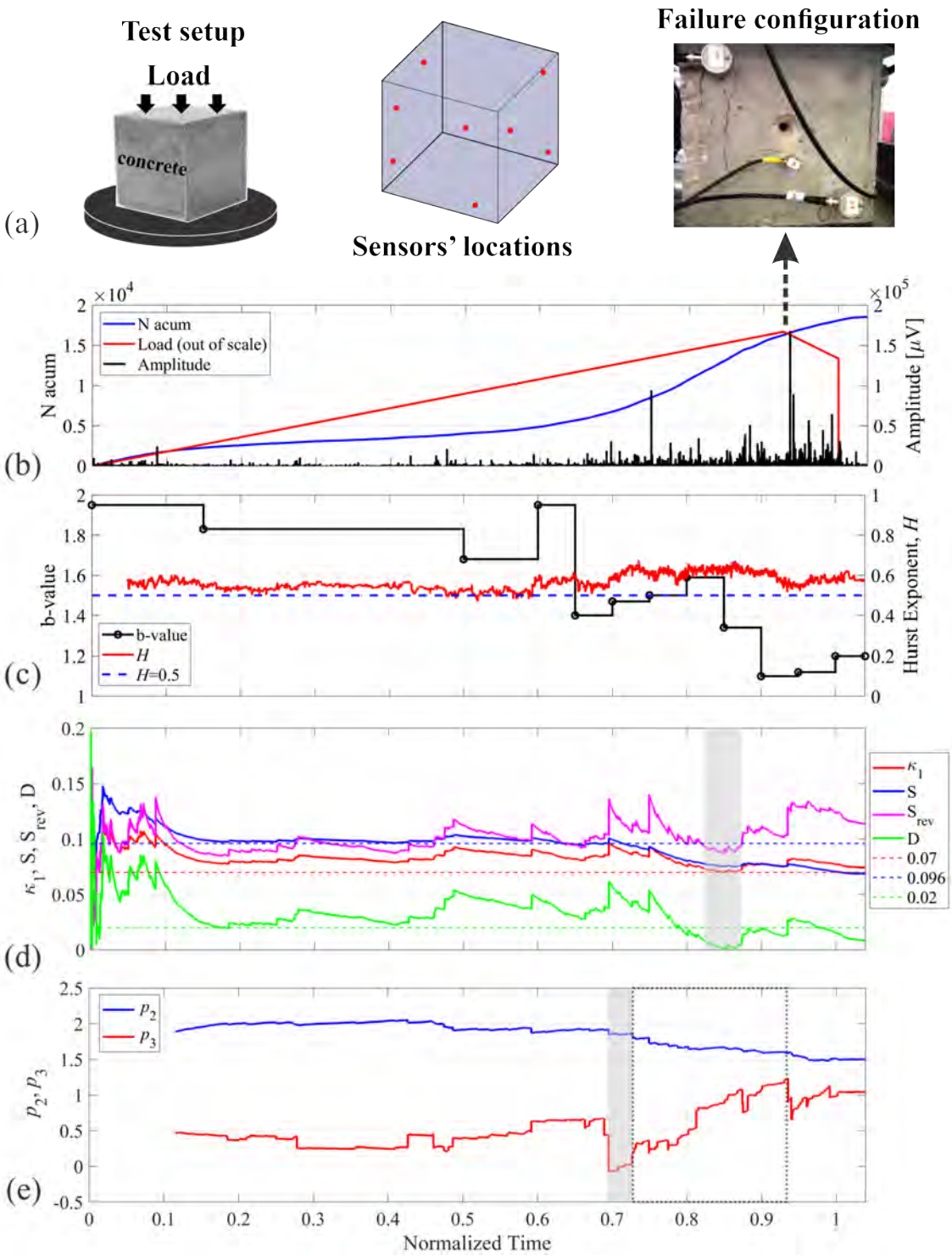

Figure 3. (a) Experimental setup of the concrete cube under compression, sensor's location and failure configuration; (b) Cumulative AE event count and AE-signal amplitudes (load is out of scale) both on the right-hand scale; (c) *b*-value and Hurst analysis;

(d) NT analysis considering $Q = A^{1.5}$; (e) fitting exponents p_2 and p_3 by following the MCF-B.

Similarly to κ_1, S in the NT domain is a dynamic quantity that incorporates the sequential organization of events. It is defined as:

$$S = \langle \chi \ln \chi \rangle - \langle \chi \rangle \ln \langle \chi \rangle \equiv \sum_{k=1}^{N} p_k \chi_k \ln \chi_k - \left(\sum_{k=1}^{N} p_k \chi_k \right) \ln \left(\sum_{k=1}^{N} p_k \chi_k \right) \quad \textbf{(4)}$$

At criticality, the entropy must fall below the value corresponding to uniform noise (S_u), i.e., $S < S_u = (\ln 2/2) - 1/4 \approx 0.0966$. To account for directional effects in event ordering, the entropy under time reversal is computed according to **Eq. (5)**, providing an additional consistency check on the evolving dynamics. The criterion for criticality is identical to that of S, specifically, $S_{rev} < S_u = (\ln 2/2) - 1/4 \approx 0.0966$.

$$S_{rev} = \sum_{k=1}^{N} p_{N-k+1} \chi_k \ln \chi_k - \left(\sum_{k=1}^{N} p_{N-k+1} \chi_k \right) \ln \left(\sum_{k=1}^{N} p_{N-k+1} \chi_k \right) \quad \textbf{(5)}$$

The average distance $\langle D \rangle$ quantifies the average separation between the normalized power spectrum **[26,27]**,

$$\Pi(\omega) = \left| \sum_{k=1}^{N} p_k e^{i\omega \frac{k}{N}} \right|^2 \quad \textbf{(6)}$$

(where $\omega = 2\pi\phi$ ($\phi \in (0, 0.5)$ denotes the natural-time frequency) and the theoretical (ideal) spectrum expected at criticality,

$$\Pi(\omega)_{ideal} = \frac{18}{5\omega^2} - \frac{6\cos\omega}{5\omega^2} - \frac{12\sin\omega}{5\omega^3} \quad \textbf{(7)}$$

which, for $\omega \to 0$, reduces to $\Pi(\omega)_{ideal} \approx 1 - 0.07\omega^2$. A system is interpreted as approaching a critical condition when the average distance between the observed spectrum and the theoretical prediction satisfies $\langle D \rangle = \left\langle \left| \Pi(\omega) - \Pi(\omega)_{ideal} \right| \right\rangle < 10^{-2}$.

In practical terms, a critical regime is inferred only when variance, entropy measures, and average spectral distance simultaneously approach their respective reference values.

Interpretation: **Figure 3(d)** presents the NT analysis performed according to the procedure described above. The onset of imminent instability is identified at the instant when all four criteria are simultaneously fulfilled (gray shaded regions). For the compressed concrete cube, this convergence occurs shortly before the peak load is reached, specifically around 0.89 in normalized time. Therefore, the NT indicators signal the transition to a critical regime immediately prior to macroscopic failure.

(d) MCF-B approach

Definition: The Method of Critical Fluctuations-Based (MCF-B) is employed to examine the statistical properties of the amplitude distribution of AE events **[32]**. It extends the conceptual basis of the original MCF **[33]**, which was designed to investigate critical fluctuations near second-order equilibrium phase transitions **[34]**. The MCF-B methodology adapts this theoretical background to AE datasets by representing the frequency–magnitude distribution

through a hybrid analytical form that incorporates both power-law (p_2) and exponential (p_3) contributions. Specifically, the distribution of AE event magnitudes is expressed as:

$$N(A) = p_1 \cdot A^{-p_2} \cdot e^{-Ap_3} \quad \textbf{(8)}$$

where p_1 is a constant. In the present study, p_3 is reported normalized with respect to the maximum amplitude within the analysed AE dataset.

Tracking the evolution of p_2 and p_3 during loading provides insight into the progressive departure from linear scaling (pure power-law) and its connection with the onset of failure. Notably, close to collapse, the behaviour of these exponents reveals a crossover pattern, comparable to transitions reported in other dynamic systems such as the Fiber Bundle Model (FBM) and fuse networks **[35,36]**.

Interpretation: **Figure 3(e)** presents the results of the MCF-B analysis applied to the AE data from the compressed concrete cube. The exponents p_2 and p_3, obtained from fitting **Eq. (8)**, are shown together with the coefficient of determination R^2 (on the right-hand axis). Up to a normalized time of approximately 0.7, both exponents remain nearly constant ($p_2 \approx 1.95$, and $p_3 \approx 0.48$). Beyond this point, the distribution converges to an almost ideal power-law regime ($p_2 > 1$, and $p_3 \approx 0.0$), highlighted in gray, indicating the emergence of scale invariance. Subsequently, a crossover behavior develops: p_2

decreases while p_3 increases monotonically as the system approaches peak load. Within the MCF-B framework, the onset of criticality is therefore characterized by the appearance of a near-perfect power law followed by the simultaneous decrease of p_2 and growth of p_3, signaling the transition to failure.

3.2. Fiber Optical Sensors (FOS)

In order to facilitate continuous monitoring of vertical deformations at the base of the Garisenda Tower, a system based on OSMOS fiber optical strands sensors was utilised (OSMOS Group is a SHM Company based in France). This system was installed in a vertical orientation on the internal faces of the structure **[7-9]**. This configuration facilitates the high-resolution detection of micrometric variations in deformation occasioned by mechanical or thermal actions, therefore, contributing to the diagnosis of the structural behaviour of the base.

The system was initiated on 31 May 2019 and consists six optical strands: four of which, measuring 2.0 m in length, were affixed to the four internal corners of the structural cell, while the remaining two, each 1.0 m in length, were positioned on the internal east and south faces, regions that lie furthest from the neutral axis and consequently experience heightened stresses **[7,8,14]**. This configuration enabled the capture the localized effects of differential deformations. **Figure 4(a)** illustrates the layout of the

optical fibers installed within the tower, while **Figure 4(b)** shows their placement along the East wall at the base.

The sensing system operates with a strain resolution of 1με and a sampling rate of 100 Hz. Data are processed in real time by an intelligent acquisition unit responsible for signal pre-conditioning, temporary storage, and transmission to a dedicated cloud platform. Access to the data is facilitated by means of a web interface, thereby enabling remote and continuous monitoring of the tower's structural performance **[7,8,14]**.

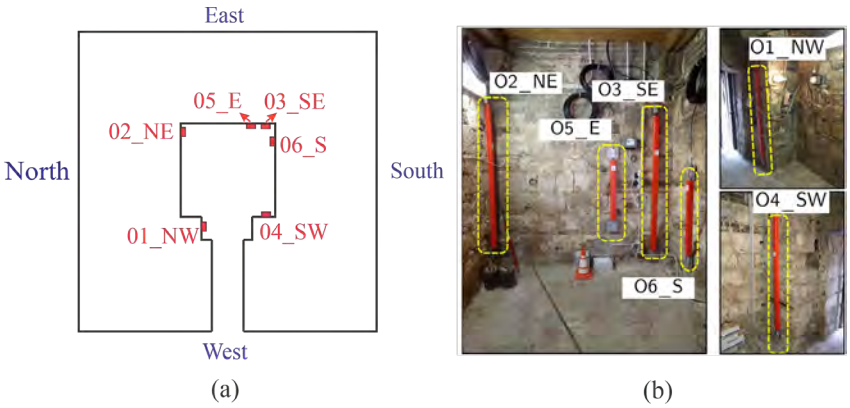

Figure 4. (a) Schematic disposition of the optical strands, (b) the optical strings installed along the eastern wall at the base of the tower.

3.3. Pendulum Monitoring

On 25 February 2021, a 30-metre long pendulum was installed by the Firm R.TEKNOS of Bergamo (Italy) within the Garisenda Tower with the purpose of monitoring horizontal movements at the tower's summit, with a particular focus on the XY plane. **Figure 5(a)** shows a

schematic representation of the pendulum system installation and **Figure 5(b)** show details of the pendulum inside the tower.

The acquisition system linked to the pendulum automatically takes measurements at six-hour intervals, transmitting the data to a management and storage platform. The device has been demonstrated to have the capacity to record displacement ranges of up to 100 mm in the x direction (facing southeast) and 50 mm in the y direction (facing northeast). The system's resolution is 0.075% of the maximum measurement range, equivalent to 0.075 mm in the x direction and 0.0375 mm in the y direction, ensuring high accuracy in detecting structural oscillations.

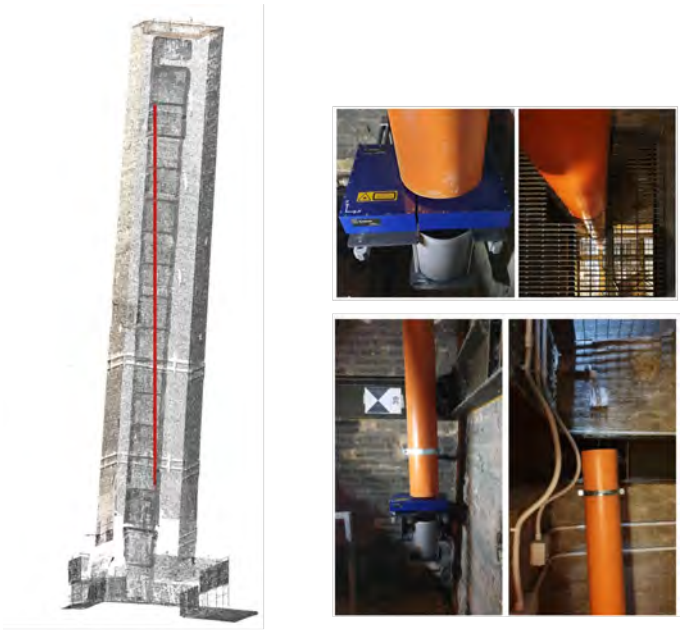

(a) (b)

Figure 5. (a) Schematic view of the pendulum installed within the tower (courtesy of R.TEKNOS); (b) detailed view of the device and its internal configuration.

In addition to displacements, the system also records the temperature within the base of the tower, measured by a sensor installed on the eastern wall approximately 0.35 m above floor level, thus allowing for the evaluation of possible correlations between thermal variations and the structure's dynamic response.

4. RESULTS AND DISCUSSION

4.1 Acoustic Emission Results

4.1.1 AE activity analysis

The AE monitoring, presented in this paper, concerns the analysis of AE signals, commencing on 31/05/2019 and concluding on 30/06/2025. More precisely, the total number of different days considered in this study is 1600, which is equivalent to the number of monitored days per year (considering both devices) as presented in **Table 1**. The number of AE events in each year is presented as well.

Table 1. Number of days monitored and AE events using devices AE001 and AE002.

Year	Monitored days AE001 (AE events)	Monitored days AE002 (AE events)
2019	92 (219)	-
2020	230 (935)	-
2021	234 (1252)	-
2022	239 (1250)	-
2023	289 (3001)	128 (1399)
2024	243 (10102)	259 (5659)
2025	158 (4488)	124 (3550)

Figure 6(a) shows the analysis of AE activity during the monitoring period. The x-axis represents the sequential day count starting from the day of the first measurement (day 151, corresponding to May 31, 2019). For subsequent years, days were added cumulatively without resetting at the beginning of each calendar year. Vertical dashed lines indicate the first day of each year, with the corresponding year labels shown above the figure. The behaviour of the accumulated number of events seems to indicate the steady growth of AE signals from AE001 up to day 1574 when exponential growth takes place, indicating a new scenario in the damage process of the structure. Due to this fact, on October 30, 2023 (day 1757 in **Figure 6(a)**) the tower was closed to visitors and the square around it (Piazza di Porta Ravegnana) was isolated by the city council to assess its structural condition **[37]**. With regard to the findings of system AE002, it is evident that it deviates from system 001 following the onset of 2024, exhibiting non-linear behaviour, similarly to AE001, although with divergent trends. For example, between the days 2000 and 2200, system AE002 exhibited no correlation with the substantial increase in accumulated AE events of system AE001. This finding suggests that the two systems are monitoring distinct sources, attributable to their different positioning within the tower.

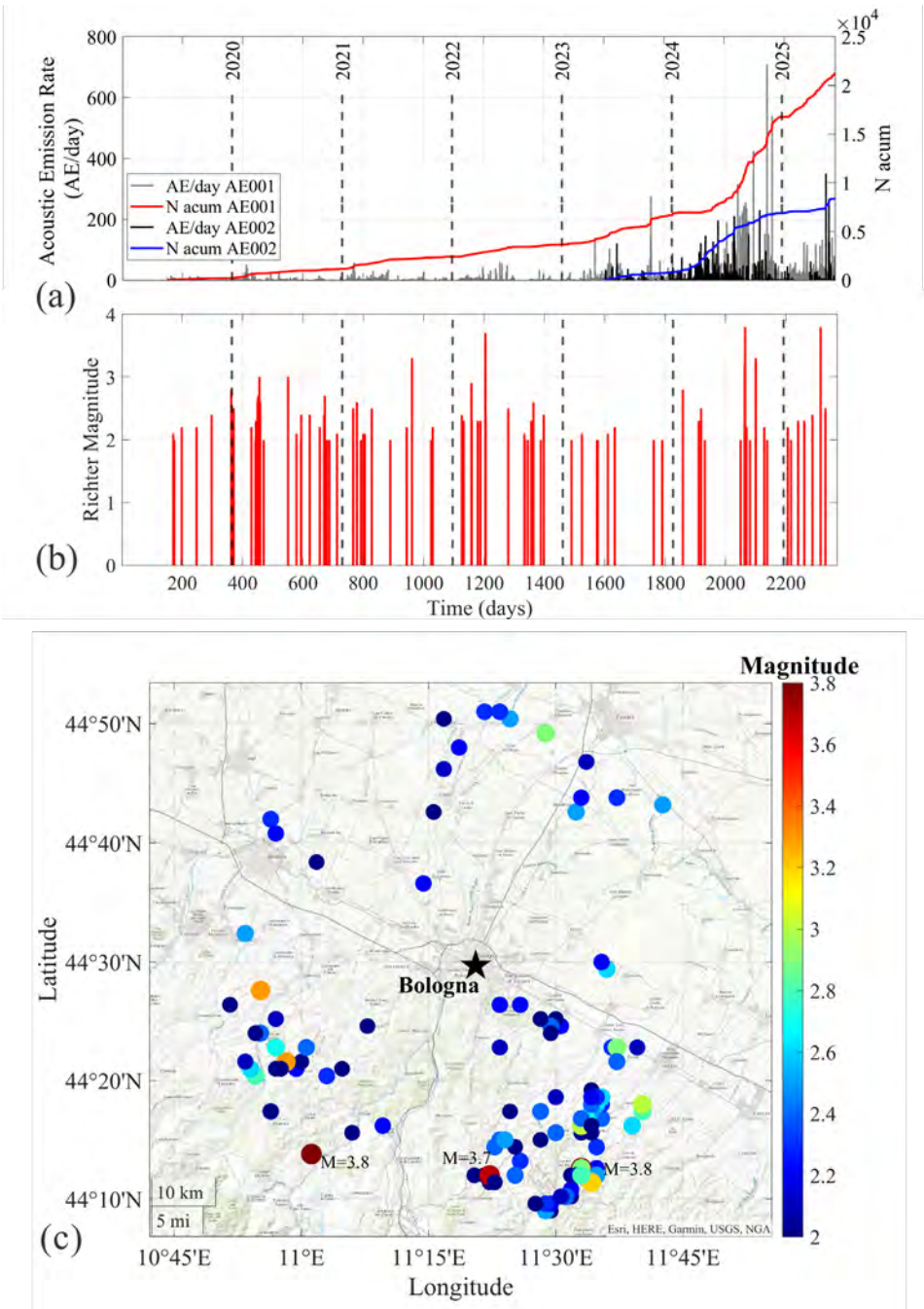

Figure 6. (a) AE Rate (AE/day) during the entire monitoring period and accumulated number (Nacum) of AE, and (b) Number of earthquakes, represented by their magnitude on the Richter scale, (c) Spatial distribution of EQs with magnitude greater or equal to 2, with the radius considered being 40 km from the city center of Bologna (data from https://terremoti.ingv.it/).

Figure 6(b) shows the number of Earthquakes (EQs) with magnitudes (M) greater than 2.0 on the Richter scale, and with epicentres located within a radius of 40 km from the city centre of Bologna. The data presented here were obtained from the Italian National Institute of Geophysics and Volcanology (INGV), and include a total of 113 EQs.

Figure 6(c) illustrates the spatial distribution of these events, with emphasis placed on those with magnitudes exceeding 3.5. During a 59-day monitoring period, temporal coincidences between local seismic events and AE activity were identified. However, the majority of these coinciding days exhibited relatively low AE rates. In fact, no consistent or immediate increase in AE activity was observed following seismic events. This finding is supported by previous reports and illustrated in **Figure 7**, which shows AE behaviour from system AE001 surrounding the M 3.8 earthquake on 26 August 2024 (day 2065 on **Figure 6(a)**), see details of this seismic event in https://terremoti.ingv.it/event/40210311 (accessed on 16 December 2025).

Despite the absence of a sudden increase at the precise moment of the seismic occurrence (01:45), a gradual growth in AE rate is observed in the subsequent hours. This suggests that, rather than exerting a direct and immediate structural impact, low-magnitude seismic events may contribute indirectly to the initiation or progression of micro cracks, potentially with a time delay as the structure seeks a new equilibrium. Therefore, while the presence of

seismic events near Bologna is recognized, the evidence indicates that they are unlikely to have significantly affected the tower's integrity during the monitoring period. Consequently, the correlation between AE and seismic activity should not be interpreted as causation, particularly in view of the low energy typically associated with the majority of recorded events.

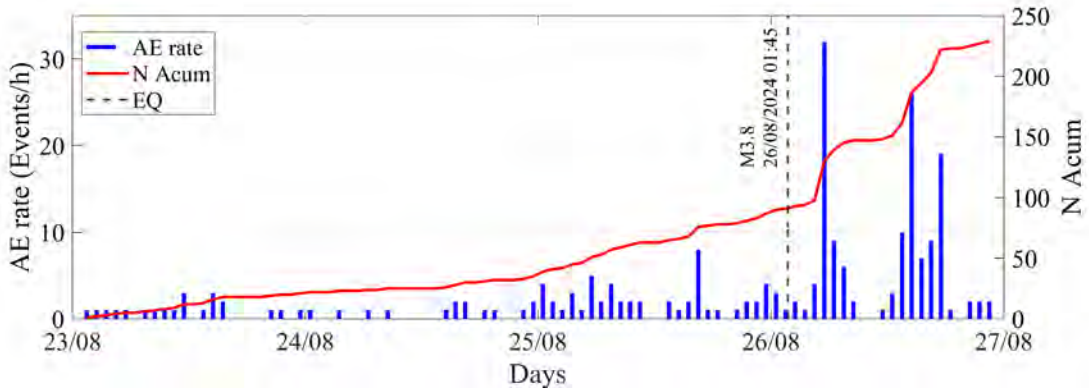

Figure 7. AE behaviour from AE001 system surrounding the M 3.8 earthquake on 26 August 2024 (day 2065 on **Figure 6(a)**), see details of this seismic event in https://terremoti.ingv.it/event/40210311 (accessed on 16 December 2025).

Figure 8 presents the seasonal analysis of AE rates for AE001 system. The values represent the median (the central value that divides the distribution in half, with 50% of days presenting lower values and 50% higher) and the interquartile range (IQR) (the difference between the third and first quartiles, a measure of dispersion encompassing the central 50% of the data).

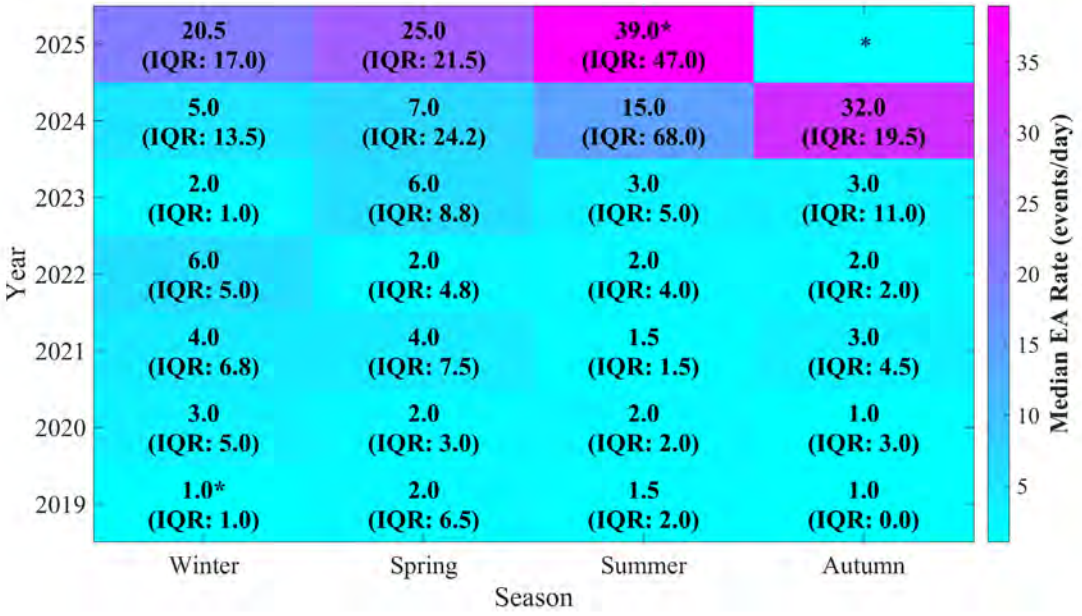

Figure 8. Seasonal analysis of acoustic emission rates (median and interquartile range - IQR) recorded by system AE001 for each year. Seasons marked with an asterisk (*) indicate incomplete data collection periods (the cell corresponding to 2025, Autumn was left empty for the same reason).

The analysis of the results reveals a clear transition in the structure's behaviour over the study period. A consistent seasonal pattern is observed between 2019 and 2022, with greater activity in winter (medians of 3-6 events/day) and lower activity in summer (1-2 events/day). This is characteristic of structures with stable thermal behaviour, where the thermal inertia of the materials predominates. However, from 2023 onwards, a progressive inversion of this pattern is identified, culminating in 2024-2025 with significantly high activity in summer (medians of 15-39 events/day)

and extreme variability (up to 68 events/day). The loss of the characteristic seasonal pattern—particularly the disappearance of winter peak activity—indicates a fundamental change in the structure's thermal resilience. This suggests the activation of damage mechanisms that are no longer directly governed by seasonal temperature variations. For instance, the propagation of cracks, rather than interfacial friction, could generate distinct acoustic emission signatures. In addition, modifications in the structural integrity may have created new stress concentration points that respond differently to thermal gradients.

Figure 9 presents the seasonal analysis of AE rates for AE002 system, which covers a shorter monitoring period (2023–2025). The figure is plotted in the same patterns of **Figure 8**. Unlike AE001, which captured the transition, AE002 data already reflect the unstable regime. AE rates were relatively low in 2023, with sporadic peaks, but increased markedly in 2024, reaching seasonal medians of ~15 events/day and high dispersion (IQR up to 33.5). In 2025, the pattern remained unstable, with variable medians and a summer peak. Overall, AE002 reveals a consistently unstable regime, characterized by moderate-to-high activity and substantial variability.

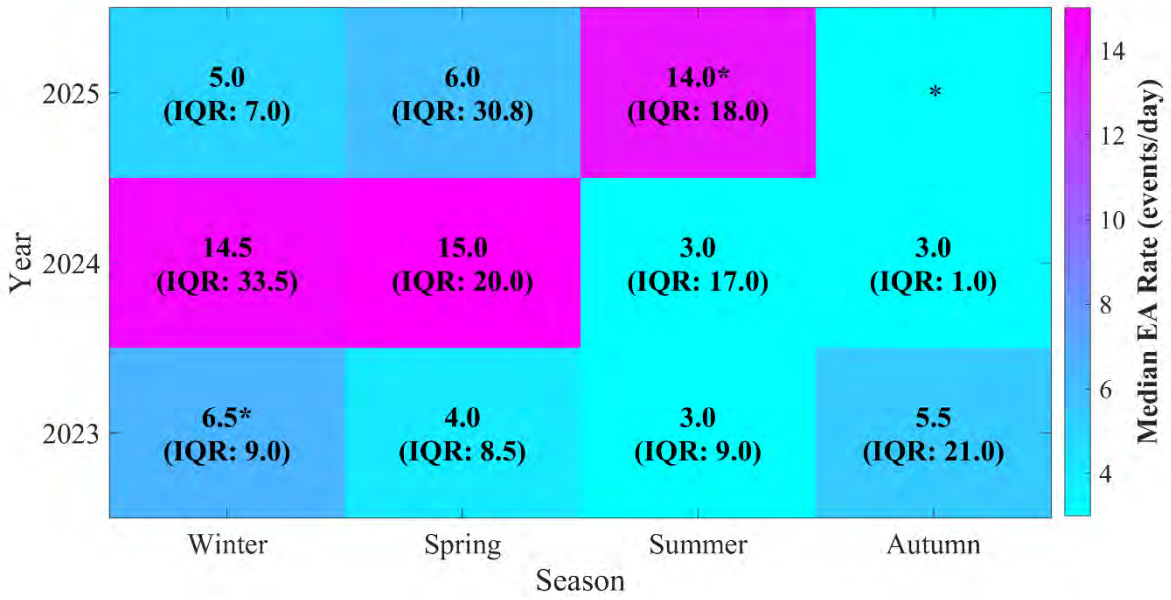

Figure 9. Seasonal analysis of acoustic emission rates (median and interquartile range - IQR) recorded by system AE002 for each year. Seasons marked with an asterisk (*) indicate incomplete data collection periods.

A comparison between the two systems reveals their complementarity in relation to AE001. AE001, which spans a longer period (2019–2025), documents the transition from a stable regime (2019–2022) to a more irregular and intensified one from 2023 onward. The AE002 system, conversely, commences precisely at this transition phase (early 2023), capturing exclusively the already unstable regime of the structure.

4.1.2 Critical behavior identified based on AE time series

The structural integrity of the Garisenda Tower is investigated by following the parameters described in Sub-section 3.1.2. It is

important to note that between 31/05/2019 and 23/01/2022, only the number of signals was recorded in the AE001 system. However, from 24/01/2022 onwards, the following AE signal parameters were stored: peak amplitude, A (mV); AE energy, E_{AE} (mV); ring-down count (number of times the AE signal exceeds a preset threshold); duration (s); and frequency, F (kHz). Such parameters were recorded by the AE002 from the point at which the system was installed.

(a) *b*-value and Hurst analysis

The *b*-value is evaluated throughout the monitoring period, considering an event moving window, *W*, equal to *W*=300 hits (that is, *b*-value is computed at event #300, based on a temporal series starting at event #1, then from #2 to #301, #3 to #302 and so on). The amplitudes of the AE signals are plotted in **Figure 10(a)** and **(b)** for systems AE001 and AE002, respectively, whereas the results of the *b*-value are presented in **Figure 10(c)**. More precisely, for AE001 a stable behavior is reported up to day 1554, with *b*-values around 1.2. It is worth remembering that *b*-values close to unity correspond to the growth of macro-fractures in the monitored element **[19]**. After that a high fluctuation in the *b*-value is reported, not being possible to recognize a trend in the fracture process. The final period with high *b* values (>2.0) suggests that the structure is stable and governed by AE events with small amplitudes. This could perhaps indicate that previous episodes are correlated with local instabilities.

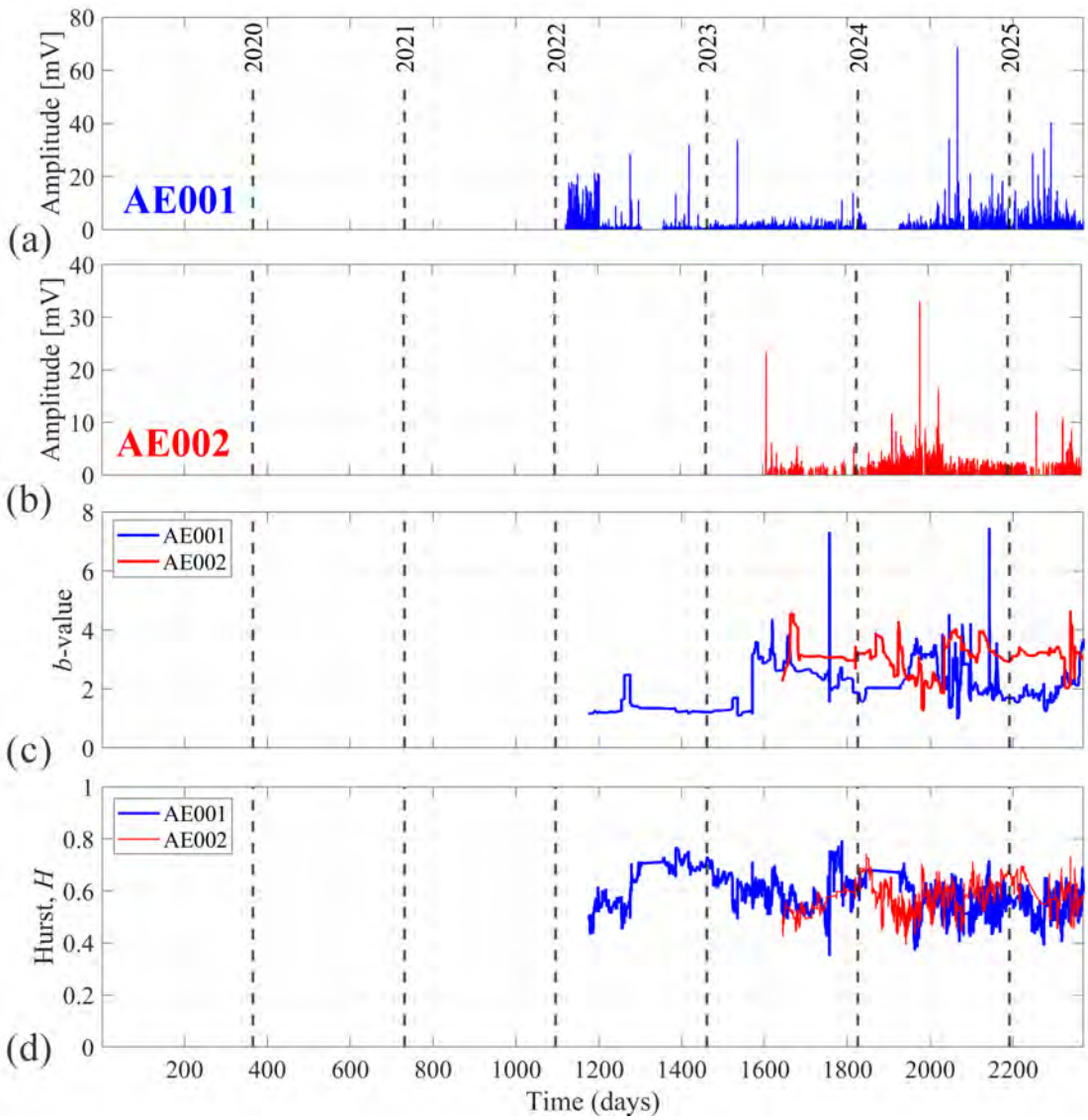

Figure 10. (a) AE amplitudes during the monitored period for AE001 and (b) AE002 systems. (c) b-value over time calculated using an event moving window, W, of W=300 events (d) Hurst exponent by using the same event moving window, W.

In contrast, the b-values reported by AE002 are consistently higher, with an average of approximately 3.2 throughout the monitoring period. This indicates a fracture process dominated by micro crack formation and the absence of significant energy releases,

suggesting a different mechanical behavior or stress environment captured by this system.

Figure 10(d) summarizes the corresponding AE signal long-range analysis according to the R^*/S^* method for both systems. The H exponent is evaluated for each event throughout the monitored period, considering a 300-event moving window, that is, by using the same approach of *b*-value. In both AE001 and AE002, persistent correlations dominate the AE signal evolution, with H values generally above 0.5. The maximum persistence is recorded at day 1773 (09/2023) for AE001 (H = 0.77) and at day 1846 (01/2024) for AE002 (H = 0.74). These values indicate that the AE processes exhibit long-term memory and that micro crack interactions may occur in a correlated manner over extended periods. **Figure 11** presents the amplitude distribution of AE events recorded by system AE001, corresponding to the signal series shown in **Figure 10(a)**. The histogram reveals that most AE events exhibit low amplitudes throughout the monitoring period. This observation supports the persistent behavior identified in the Hurst analysis (**Figure 10(d)**), suggesting that small-amplitude events are temporally correlated and likely to be followed by other small events. In other words, the high Hurst exponent may not be attributed to energy escalation, but rather to the structured recurrence of low-energy activity. Only the data from AE001 are used in this example, given its more extensive and continuous recording period compared to AE002.

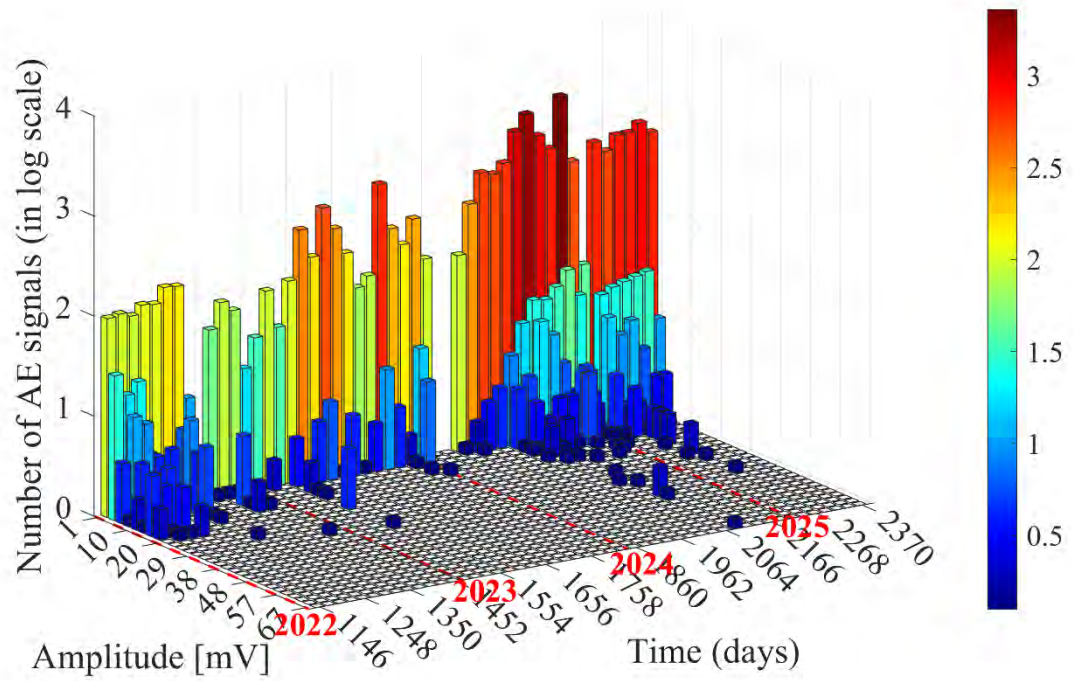

Figure 11. Distribution of AE event amplitudes plotted in **Figure 10(a).** The color scale represents the accumulated number of AE signals in log scale.

(b) Natural time approach

The NT was employed taking the energy parameter Q_k equal to $A^{1.5}$, where A is the maximum amplitude of the signal (in *m*V). Calculation of the term $A^{1.5}$ was performed hit by hit, i.e., every time a new signal was identified, it was included in the NT analysis, leading to the rescaling of the (χ_k, Q_k) time series and the recalculation of κ_1, S, S_{rev} and <*D*>. The figure additionally includes horizontal reference lines marking the critical values of κ_1 (red dashed), <*D*> (green dashed), and the entropies S and S_{rev} (blue dashed). In the

present framework, the system is considered critical only when all four indicators simultaneously attain their respective thresholds. The time interval satisfying these conditions is highlighted in gray in **Figure 12**. By contrast, the yellow region corresponds to intervals where one of the NT parameters has not yet reached its critical value.

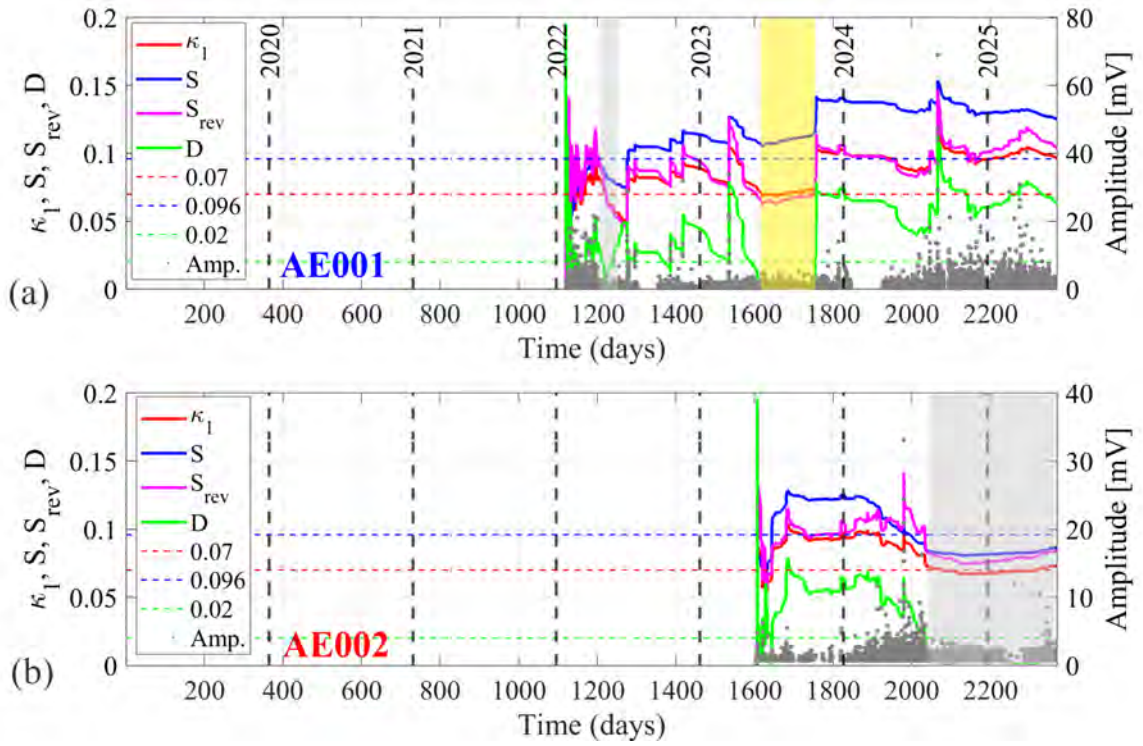

Figure 12. Natural time approach by employing $Q_k = A^{1.5}$ for system (a) AE001 and (b)AE002. A grey background is indicative of a critical regime, whereas a yellow background signifies that the entropy parameter (S) has not exceeded a critical value.

It can be seen that, for AE001 system, **Figure 12(a)**, the first critical region occurs on day 1207 before the occurrence of AE

activity with high amplitude events (the b-value is also close to 1 on this day, see **Figure 10(b)**). The second critical region assumed (only the entropy S did not converge), is a wider region between days 1619 (06/2023) and 1758 (10/2023). The beginning of this second region corresponds to the one where a high AE rate is reported. After this second region, all NT parameters move away from the convergence values towards criticality, indicating that the structure is stable. Therefore, the critical regions above may suggest local instabilities. It is worth noting that the yellow region in **Figure 12(a)** might be related to the preparation for the traffic closure around the tower on day 1757 (10/2023), although this should be interpreted as a hypothesis rather than a definitive conclusion.

Regarding the AE002 system, the NT analysis identified a critical region, located from day 2050 until the last day of monitoring, that is, June 30, 2025. In the framework of NT analysis, this behavior indicates a state of enhanced correlations within the system, which may be associated with a long-term reorganization process or an ongoing search for a new equilibrium configuration at the tower base. Although both AE systems record emissions associated with the same structure, the spatial distribution and intensity of the events detected differ significantly. The difference in event density, coupled with their possible location in regions with distinct damage progressions, may explain the deviations observed in the critical parameters.

(c) MCF-B approach

To estimate the exponents p_2 and p_3 within the MCF-B framework, a sequential procedure is adopted:

1. Construct the amplitude histogram considering an initial subset of AE events from event #1 up to event #B;
2. Represent the corresponding frequency–magnitude distribution in log–log scale and fit it using **Eq. (8)** to extract p_2 and p_3;
3. Extend the dataset incrementally (from #1 to #B+1, #B+2, and so on) and repeat the previous steps, allowing the continuous updating of the exponents throughout the entire record.

Within this methodology, the onset of criticality is identified by the emergence of an almost ideal power-law regime, followed by the concurrent decrease of p_2 and monotonic growth of p_3.

Figure 13(a) presents the results of the MCF-B approach for the AE001 system, along with the AE amplitudes (shown on the right-hand axis). An initial dataset consisting of 300 events was considered. The critical behavior mentioned above was not observed in the time series under analysis. In fact, the observed trend is the opposite of what would be expected in a critical scenario: the p_2 value increases monotonically while p_3 decreases. This competitive behavior between the exponents is characteristic of the MCF-B approach, similarly to what was originally proposed in the MCF framework.

Between days 1813 (12/2023) and 2066 (08/2024), the p_3 value approaches zero, suggesting the emergence of a perfect power-law regime, which implies that AE events are occurring across all scales. This phenomenon coincides with a phase of exponential growth in the cumulative number of AE events, as shown in **Figure 6**. After this period, negative values of p_3 are observed, indicating an upward tail in the $N(A)$- A relationship. This behavior may suggest the coexistence of multiple AE mechanisms or sources. Such findings are consistent with observations reported by Birck et al. **[38]** in the context of seismology.

One approach to identifying AE emission sources is based on the Rise Time (RT) versus Average Frequency (AF) relationship. In the absence of RT data, the analysis was instead performed using the Duration versus AF relationship. **Figure 13(b)** presents the evolution of the characteristic frequency and duration of AE events, calculated using a moving average of 20 samples. After 2024, a decline in the frequency of AE events is observed, accompanied by an increase in the duration of AE events. This trend may indicate the activation of shear-related failure mechanisms. However, a more precise interpretation would benefit from RT measurements, which were not recorded in this dataset. At the same time, the tendency for the characteristic frequency of AE events to decrease may represent an increase in the flexibility of the structure in the local of the AE sensors, therefore associated with the loss of a more stable condition.

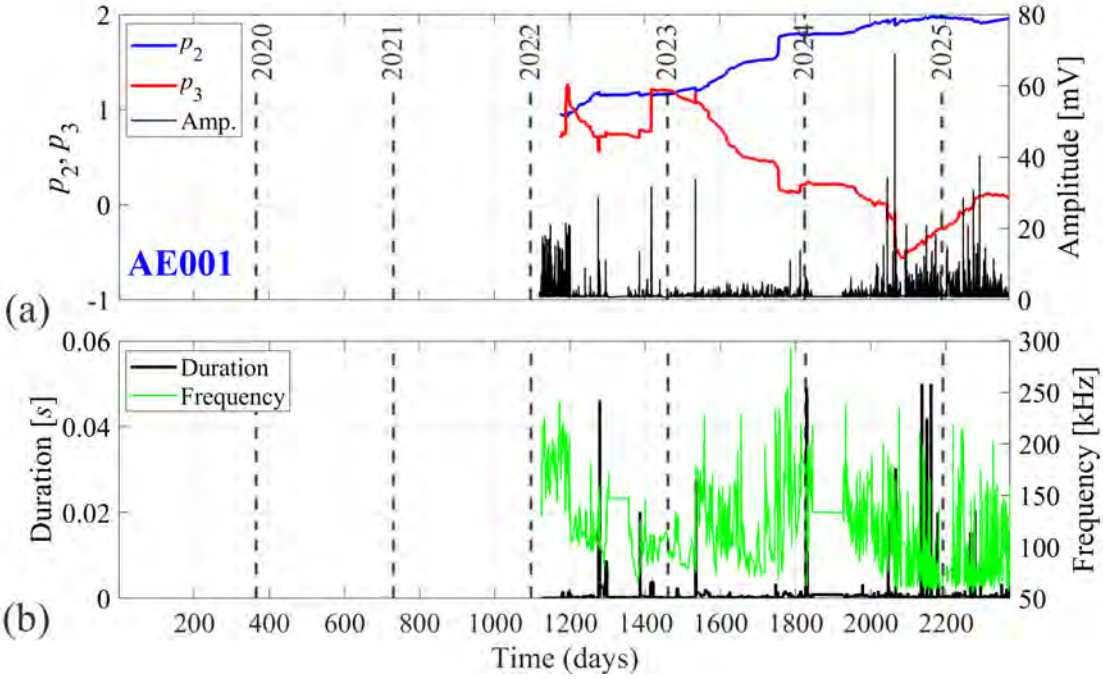

Figure 13. For AE001 system: (a) Exponents p_2 and p_3, and (b) Frequency and duration of AE signals starting on 01/24/2022.

Figure 14(a) presents the results for the AE002 system, following the same procedure employed to compute the exponents for the AE001 system. It can be observed that the critical MCF-B signature is identified in the AE002 data. More precisely, this critical region starts shortly after the activation of the AE002 system in early 2023 and lasts until approximately day 1980 (06/2024). Notably, this region occurs slightly earlier than that identified by the natural time (NT) analysis (see **Figure 12(b)**). Another important observation is that after this critical region, the value of the p_3 exponent remains approximately zero until the end of the monitored period. This indicates, as also observed in the

AE001 system, that a power-law relationship is established, suggesting that AE events occur across all length scales.

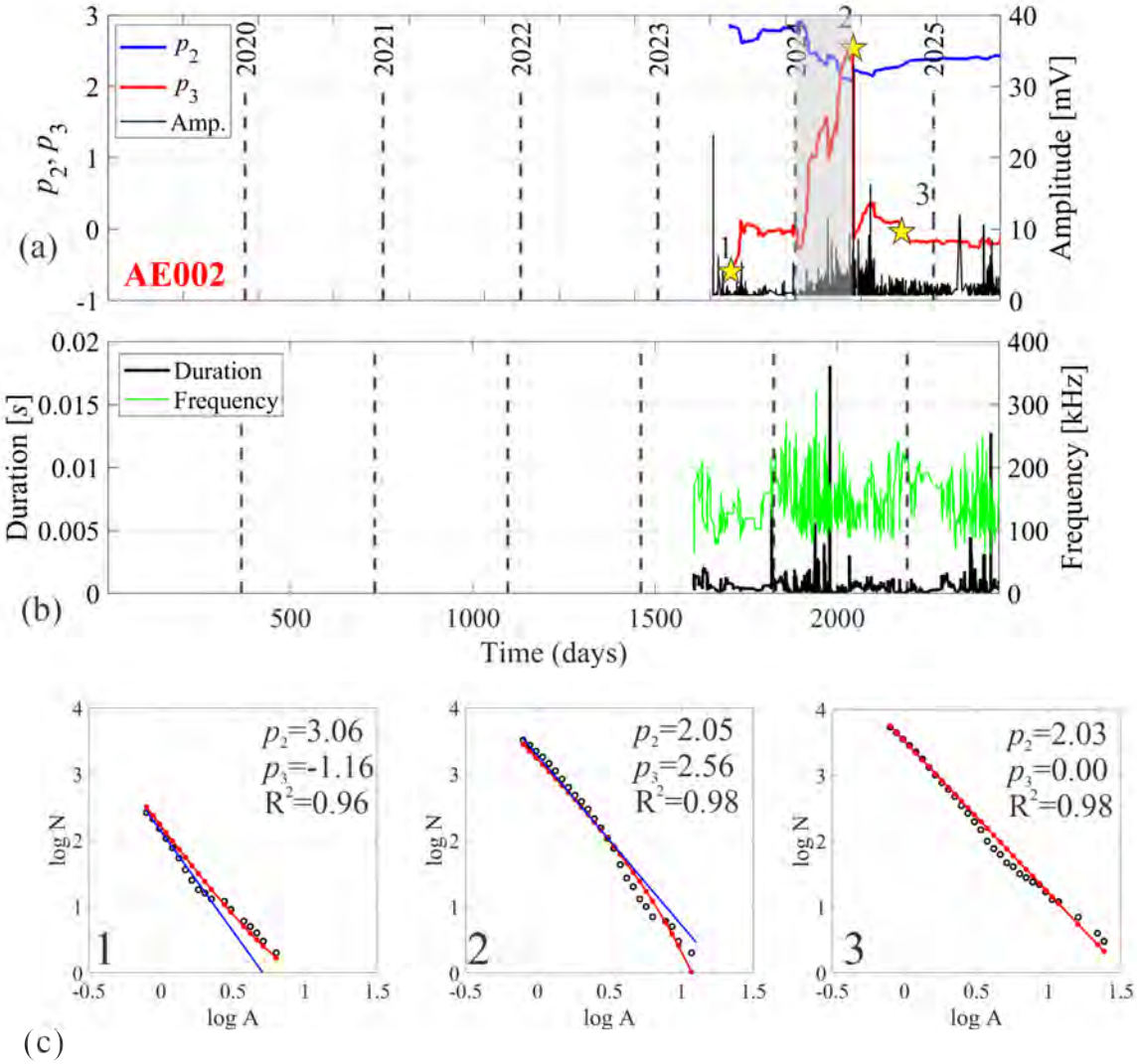

Figure 14. For AE002 system: (a) Exponents p_2 and p_3 from the MCF-B approach, and (b) Frequency and duration of AE signals starting on 01/24/2023. (c) Evolution of exponents p_2 and p_3, together with the coefficient of determination, R^2, for days (a) 1652, (b) 1978 and (c) 2119 in **Figure 14(a)**. The solid blue line is the linear approximation.

Regarding the duration and frequency of the signals, which are presented following the same format used in **Figure 14(b)**, no significant changes in behavior are observed throughout the monitored period.

Figure 14(c) details the fitting procedure used to generate **Figure 14(a)**, focusing on days 1652 (11/07/2023), 1978 (31/05/2024), and 2119 (17/10/2024), identified in **Figure 14(a)** by yellow stars. The exponents were estimated using the fitting function described in **Eq. (8)**, with the coefficient of determination (R^2) included in each subplot of **Figure 14(c)**. It is noteworthy that point 3 in **Figure 14(c)** reveals a "perfect" power-law behavior, whereas the other cases show a deviation from linearity.

4.2. FOS Results

Figure 15 shows the average daily strain, calculated by averaging the measurements from the five optical strands, as a function of the average daily temperature recorded inside the tower cell. The results reveal an approximately linear correlation, consistent with thermo-mechanical effects, being the greatest contractions occurring around 8.0°C, while the largest expansions observed near 25.0°C. Over time, the dataset gradually shifts towards more negative strain values, suggesting the accumulation of long-term structural deformation superimposed on seasonal cycles. A small deviation is observed at the beginning of the monitoring period, which might be related to

sensor accommodation or transient conditions immediately after installation.

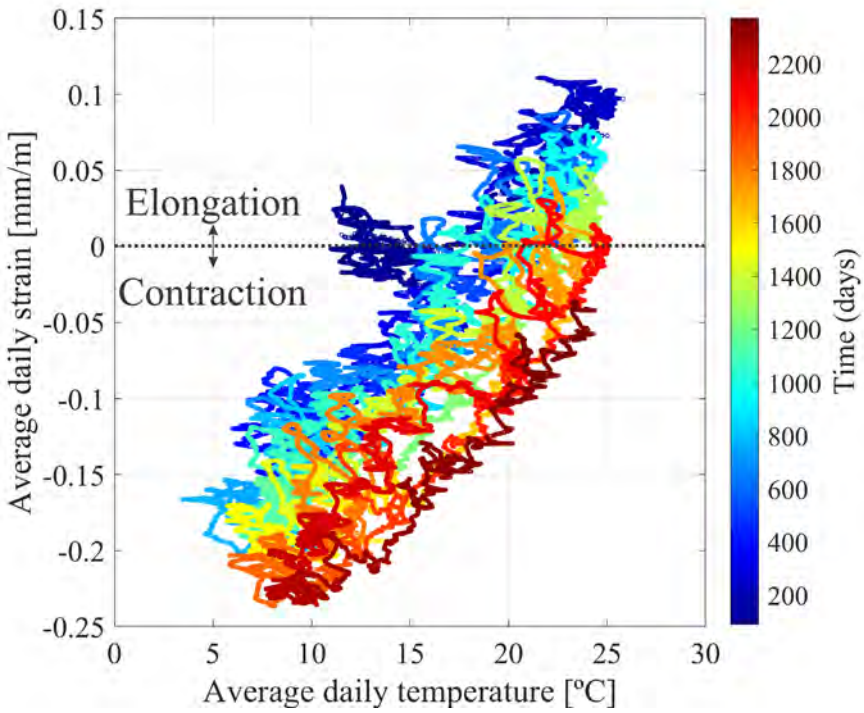

Figure 15. Correlation between walls average vertical strains measured by five FOS and tower internal temperature.

Figure 16 shows the temporal evolution of FOS measured along with the cumulative number of AE events from both AE systems (see the disposition of each FOS within the tower in **Figure 4**). The strain curves exhibit a cyclic pattern consistent with seasonal influences; moreover, they also display significant non-recoverable part of the strains during the final phase of monitoring, especially in the SE direction (FOS O3), that coincide temporally with the phase of exponential AE growth.

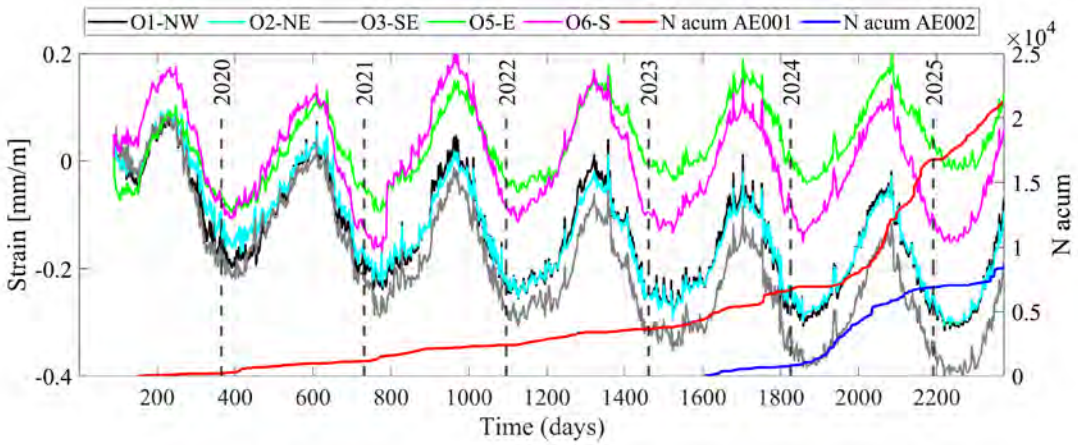

Figure 16. Temporal evolution of the strains reported by FOS, together with the accumulated number of AE events (on the right-hand scale) for both AE systems.

By analyzing the strains trends shown, it is evident that the minimum contraction values are recorded by the optical strand O5E, positioned at the southeast corner of the tower cell. In contrast, the highest contraction values are associated with the optical strand O1NW, located at the northwest corner. This spatial distribution of strain amplitudes is consistent with the expected structural behavior of a tilted tower, where differential thermal responses and gravitational effects are more pronounced along specific orientations.

When comparing the cumulative AE signals from system AE001 with the strain trends, it is observed that the largest increases in AE activity correspond to the periods of maximum wall contraction, particularly before the year 2022. Notable examples include the abrupt AE signal rises on days 408 (January 25, 2020) and 772

(January 26, 2021), which coincide with the minimum deformation values recorded by the FOS system. However, after 2022, this correlation between contraction and AE activity becomes less evident or disappears altogether.

The correlation between the cumulated AE activity and FOS average daily strains, as well as that between the cumulated AE activity and average daily temperature, are shown in **Figure 17** and **18** for AE system 001 and 002, respectively. It should be noted that the figure is divided into two scales, separated by the light blue shadow area (0–0.35×10^4 and beyond 0.35×10^4 accumulated number of AE events), in order to emphasize the distinct features of the initial monitoring phase compared with the later structural response.

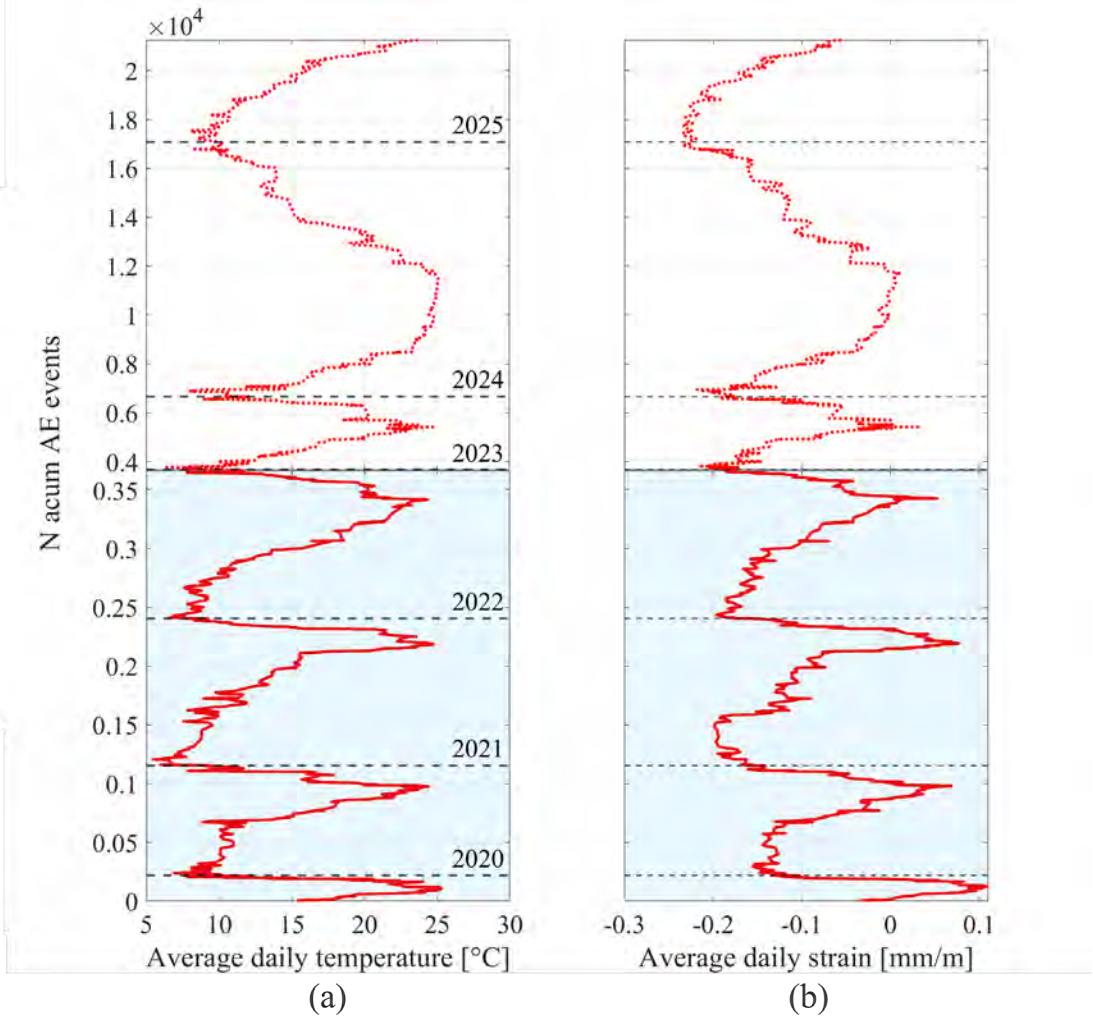

Figure 17. AE001: (a) Average daily temperature vs cumulated AE activity, and (b) average daily strain vs cumulated AE activity. The light blue shadow area (0–0.35×10⁴ and beyond 0.35×10⁴) separate the two scales used to emphasize the distinct features of the initial monitoring phase compared with the later structural response.

In the case of AE001, **Figure 17**, a clear seasonal pattern emerges, where the largest increases in AE activity predominantly occur during periods of thermal contraction of the masonry walls, especially when temperatures drop below approximately 12 °C and

average strains fall below –0.1 mm/m. This behavior can be explained by the complex internal structure of the tower’s masonry. As reported in previous studies **[7,8,14]**, the tower wall has an overall thickness of approximately 275 cm, consisting of three main components: (i) an inner layer of about 40 cm of selenite block masonry (a crystalline form of gypsum), (ii) a ~150 cm core of heterogeneous “a sacco” masonry, and (iii) an external 80 cm layer of selenite blocks, including the ashlar covering. Due to the different thermal properties and mechanical behaviors of these materials, especially the lower thermal conductivity and greater disorder of the “a sacco” masonry, the structure likely undergoes differential thermal deformation during cooling periods. While the selenite layers may contract more rapidly, the central “a sacco” core, due to its higher thermal inertia, responds more slowly to temperature changes. This mismatch may generate shear stresses at the interfaces, particularly between the rigid selenite blocks and the irregular inner core, which can lead to micro cracking and result in AE signals. Over repeated seasonal cycles, this mechanism may contribute to a fatigue-driven degradation process affecting the integrity of the tower. Notably, a change in this correlation appears after 2023, where the rate of AE accumulation becomes more uniform, potentially indicating a shift in the structural response.

Similar behavior is observed for system AE002 (**Figure 18**), where the cumulative AE events again show a correlation with colder periods and increased contraction. These repeated patterns across multiple

monitoring systems further support the hypothesis that differential thermal deformation between structural components is the primary driver of acoustic activity in the tower.

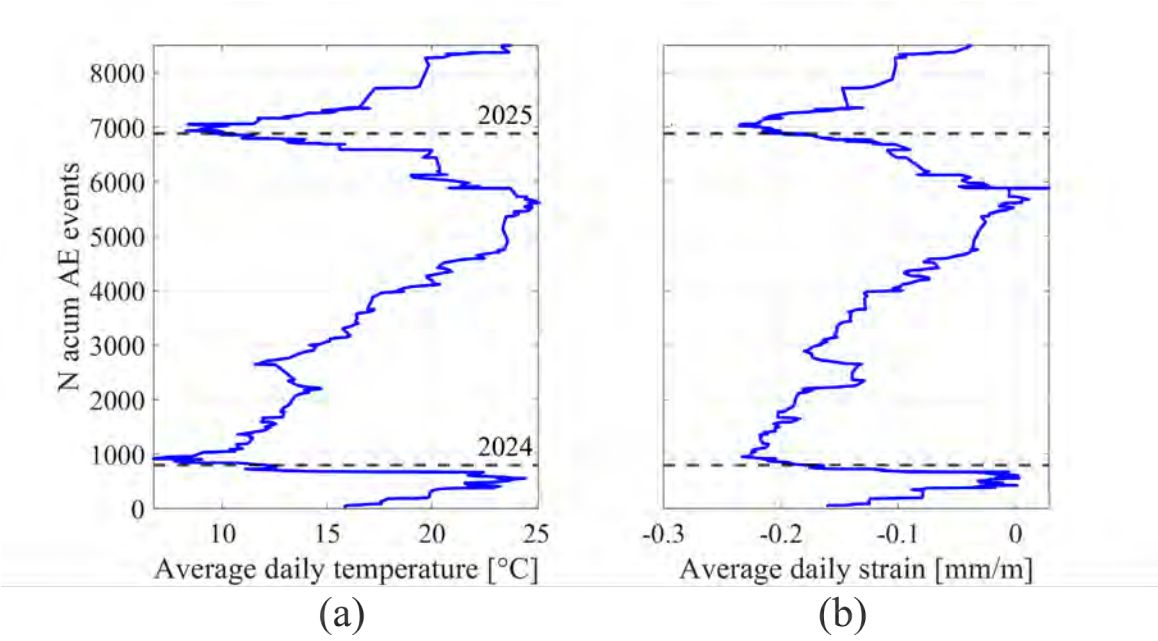

Figure 18. AE002: (a) Average daily temperature vs cumulated AE activity, and (b) average daily strain vs cumulated AE activity.

4.3. Pendulum Results

Figure 19 presents the monitoring results with the pendulum installed at Garisenda tower cell. **Figure 19(a)** shows the displacements in the East-West (pdx) and North-South (pdy) directions, along with the temperature variation (Temp) over approximately 1,600 days (from February 2021 to June 2025) together with their long-term trends. A strong correlation can be observed between temperature and the seasonal displacements of the pendulum, with contractions during the cold months and expansions during the warm months.

Figure 19(b) shows the evolution of the pendulum displacements recorded over the days of monitoring, where the red and blue solid lines are the trends of the displacements in x and y, directions, respectively. By considering the trend lines, the results indicate a cumulative drift of approximately +2.6 mm in the eastward direction (pdx) and –1.35 mm in the southward direction (pdy), which corresponds to a resultant displacement trend of about 2.9 mm towards the southeast. Short-term oscillations are evident and can be attributed to reversible effects such as thermal cycles, but the long-term trend reflects an irreversible structural movement. Overall, the pendulum measurements suggest that the tower is slowly migrating towards the southeast direction during the monitored period.

The irreversible displacements identified by the pendulum system, although small in magnitude, should be seen as early signs of structural evolution. When considered in conjunction with the wall deformation data and acoustic emission signals, these displacements suggest that the tower is undergoing a slow but continuous process of internal reconfiguration.

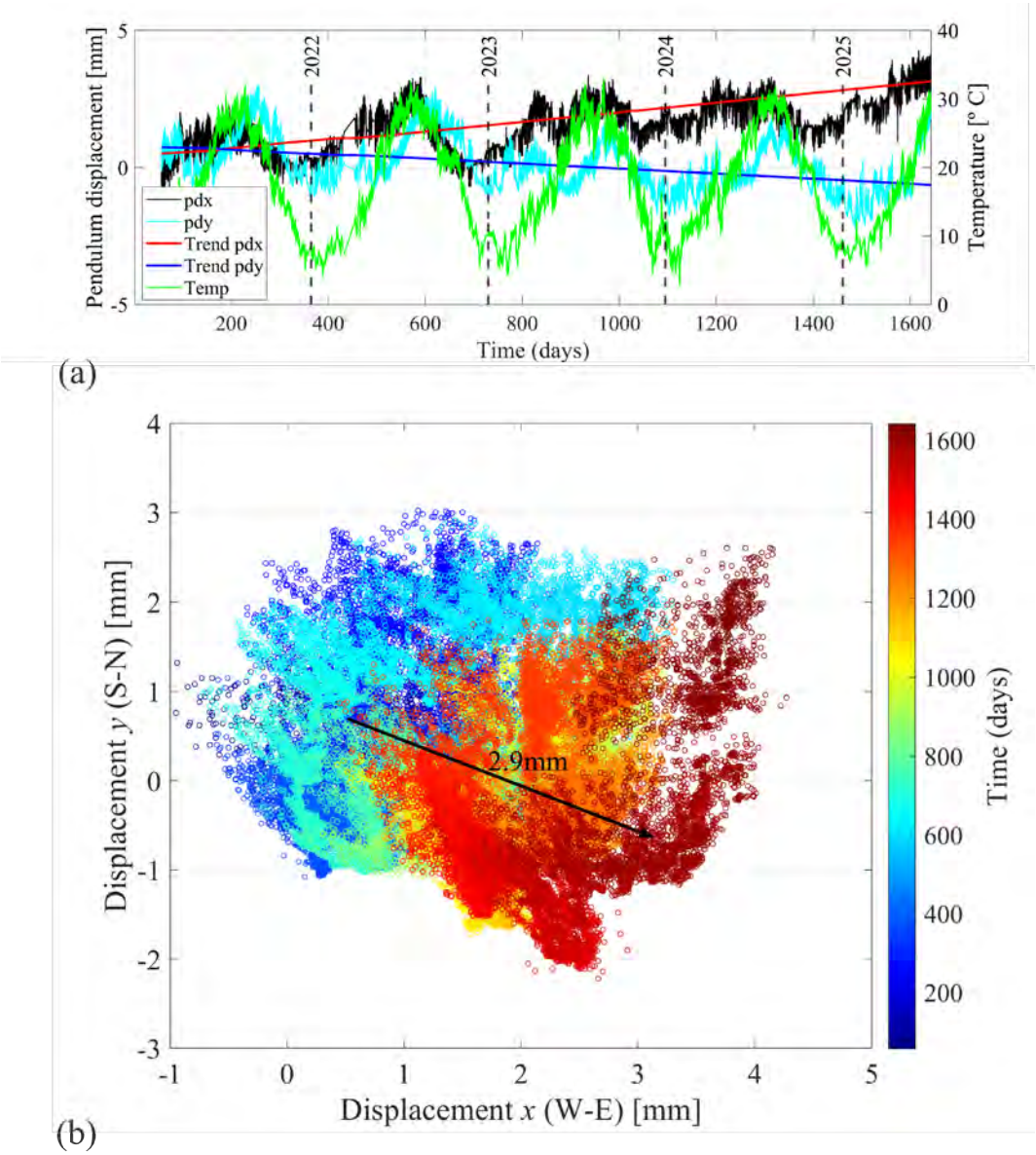

Figure 19. (a) Pendulum displacements in the x and y directions and temperature over time. (b) pendulum movement from 2021 to 2025, highlighting the displacement trend of 2.9 mm in the period.

4.4. Discussion

The integration of data from the various monitoring systems— AE, FOS, and the pendulum —combined with internal temperature

measurements, offers a comprehensive view of the structural behavior of the Garisenda Tower.

With reference to Structural Health Monitoring (SHM) data, particularly those acquired through AE, the analyses indicate the presence of signals compatible with progressive damage over time, attributable to microcracking phenomena affecting the load-bearing material.

A consistent trend emerges across all datasets: thermal cycles play a central role in driving both microstructural damage (as revealed by AE) and macroscopic deformations (as captured by FOS and the pendulum). Specifically, periods of thermal contraction, typically associated with lower temperatures, coincide with the highest AE activity rates, especially before 2022. This supports the hypothesis of differential thermal deformation between the inner and outer masonry layers of the tower, leading to shear stresses and microcracking.

The spatial distribution of AE activity further suggests that such damage processes are not uniform, but rather preferentially concentrated in specific structural zones, most notably at the selenite basement and in the lower inner masonry core on the eastern side of the tower.

The FOS data corroborate this view, showing contraction maxima in colder months, particularly in directions aligned with the tower's inclination. Notably, the SE and NW optical strands exhibit the most

extreme strain values, suggesting anisotropic deformation patterns linked to the tower’s tilt and orientation.

The pendulum records further reinforce this interpretation. The displacements show clear seasonal cycles superimposed on a slow, irreversible drift. This drift, accumulating to about 2.9 mm over 4.5 years, indicates permanent structural evolution, possibly driven by cumulative damage, material creep, or foundation settlement.

The temporal trends observed in the AE datasets therefore point to the need for a careful and cautious interpretation, framed within a continuous and evolutionary monitoring perspective, aimed at ensuring both monument preservation and public safety.

After 2022, a clear behavioral shift is observed. AE activity becomes more uniformly distributed throughout the year, even during periods without significant contraction. Several possible causes may explain this transition: (i) accumulated material degradation – repeated thermal cycles (2019-2022) may have reduced interfacial stiffness between selenite blocks and the inner “a sacco” core, altering the balance between friction and crack generation; (ii) long-term environmental effects – changes in moisture content or mean annual temperature could modify the internal thermally-induced stress fields; (iii) fatigue-driven damage – the accumulation of microcracks over multiple seasons may have reached a threshold where further damage occurs more readily even under small temperature variations. These hypotheses, however, require further targeted investigations that are currently the subject of unpublished studies

or will be explored in future work. Such a shift is supported by the emergence of power-law signatures in AE time series (as seen in the MCF-B analysis), and by the loss of correlation between strain and AE in the later monitoring period.

It should be emphasized, however, that the measurements were acquired while an active construction site was present. As a result, part of the observed signal variability may be related to ongoing works, which can induce transient perturbations on the structure without necessarily implying a permanent worsening of its structural condition.

In summary, the integrated analysis suggests that:

- From 2019 to 2022, damage progression was governed by seasonal thermal stresses, with AE peaks coinciding with winter contraction.
- A clear transition occurred around 2023, marked by: (i) loss of the characteristic seasonal AE pattern; (ii) exponential growth in cumulative AE events; (iii) emergence of power-law behaviour in the MCF-B analysis; and (iv) loss of correlation between AE and FOS strains.
- Post-2023, damage processes became more autonomous and less dependent on thermal triggers, indicating a possible regime shift toward increased instability.
- The pendulum recorded a cumulative southeastward drift of ~2.9 mm over 4.5 years, confirming irreversible structural movement.
- FOS data showed deformation with maximum contraction at the SE corner, consistent with the tower’s tilt direction.

- The two AE systems were complementary: AE001 captured the full transition (2019-2025), while AE002 (starting in 2023) only recorded the unstable regime.

These findings highlight the importance of multi-parameter monitoring for heritage structures, enabling the early detection of transitions in structural behavior that could otherwise go unnoticed in single-sensor assessments.

5. CONCLUSIONS

The structural behaviour of the Garisenda Tower has been assessed through a multiscale monitoring framework combining AE, FOS, and pendulum data. The main findings are:

-Acoustic Emission: Seasonal patterns dominated until early 2022, when contraction extremes in winter coincided with AE peaks.

-After 2022, signal irregularities and criticality indicators suggest a transition toward autonomous damage accumulation.

-Fiber Optic Sensors (FOS): Wall deformations correlated strongly with internal temperature, with maximum expansion near 25 °C and maximum contraction near 6 °C. The SE and NW strands exhibited the largest amplitudes, consistent with tilt-induced anisotropy.

-Pendulum: Recorded a slow but irreversible displacement of nearly 3 mm over 4.5 years, superimposed on seasonal oscillations, confirming long-term south-eastward drift.

- Overall, the combined results from the three independent monitoring systems indicate the presence of evolving damage-related processes,

characterized by both seasonal effects and longer-term components. These findings are intended exclusively as a statistical characterization of the monitored response and of changes in damage-related regimes, and do not imply any direct assessment of the global structural stability or safety conditions of the Tower.

The following points may assist in the continued assessment of the Garisenda Tower:

-Maintaining the multi-technique approach (AE, FOS, pendulum) is advisable, as each contributes complementary information.

-The SE base region deserves close attention, as it consistently showed higher deformation and AE activity.

-Statistical methods such as natural time and MCF-B can be useful for detecting regime shifts when applied to AE data in an off-line, expert-driven workflow.

DECLARATION OF COMPETING INTEREST

The authors declare that they have no known competing financial interests or personal relationships that could have appeared to influence the work reported in this paper.

ACKNOWLEDGMENTS

The Municipality of Bologna is acknowledged for granting permission to publish this manuscript.

The funds provided by the Municipality of Bologna to the Politecnico di Torino for the project "Monitoring by AE Technique of the

Garisenda Tower in Bologna", which enabled the research to be conducted, are duly appreciated.

CREDIT AUTHORSHIP CONTRIBUTION STATEMENT

Giuseppe Lacidogna: Supervision, Methodology, Writing- Reviewing and Editing.

Leandro F. Friedrich: Writing-Original draft preparation, Conceptualization, Investigation, Methodology, Visualization.

Pedro M. Montanari: Methodology and Writing-Review.

Mariana H. Padilha: Investigation, Methodology, Visualization.

Stefano Invernizzi: Supervision, Writing- Reviewing and Editing.

Angelo Di Tommaso: Supervision, Writing- Reviewing and Editing.

Ignacio Iturrioz: Supervision, Methodology, Writing- Reviewing and Editing.

All authors have read and agreed to the published version of the manuscript.

DATA AVAILABILITY

The data used to support the finding of this study are available from the corresponding author upon request.

REFERENCES

[1] Baraccani S, Azzara RM, Gasparini G, Morelli A, Palermo M, Trombetti T, Zaccarelli L. Identification through seismometric measurements of transients propagating inside the Asinelli and Garisenda Towers (Bologna, Italy), implication on structural modeling and state of health monitoring. Eccomas Proceedia COMPDYN 2019;3881–3892. doi:10.7712/120119.7193.19071.

[2] Baraccani S, Piccolo A, Gasparini G, Palermo M, Trombetti T. An assessment of the structural behaviour of the Garisenda Tower in Bologna through finite element modelling and structural health monitoring. Eccomas Proceedia COMPDYN 2019;5416–5422. doi:10.7712/120119.7314.19061.

[3] Cavani F. Movimenti della sommità rispetto alla base nella torre Garisenda di Bologna. Memorie della Regia Accademia delle Scienze dell'Istituto di Bologna – Classe di Scienze Fisiche 1901; VII:317–330.

[4] Dallavalle G, Di Tommaso A, Gottardi G, Trombetti T, Lancellotta R, Lugli S. The Garisenda Tower in Bologna: effects of degradation of selenite basement on its static behaviour. In: Lancellotta R, Viggiani C, Flora A, de Silva F, Mele L, editors. Geotechnical Engineering for the Preservation of Monuments and Historic Sites III. London: CRC Press; 2022. p.1088–1100.

[5] Pesci A, Casula G, Boschi E. Laser scanning the Garisenda and Asinelli Towers in Bologna (Italy): detailed deformation patterns of two ancient leaning buildings. J Cult Herit 2011;12(2):117–127.

[6] Poluzzi L, Barbarella M, Tavasci L, Gandolfi S, Cenni N. Monitoring of the Garisenda Tower through GNSS using advanced approaches toward the frame of reference stations. J Cult Herit 2019; 38:231–241.

[7] Di Tommaso A, Olivetti GC, Niccolini G, Lacidogna G, Borla O, Carpinteri A. Garisenda Tower in Bologna (Italy): health monitoring by different nondestructive testing techniques. Int J Masonry Res Innov 2022;9(1–2):54–66.

[8] Di Tommaso A, Olivetti GC, Lacidogna G, Invernizzi S, Carpinteri A. Garisenda tower in Bologna (Italy): Structural assessment and numerical simulation. Int J Masonry Res Innov 2024;9(4):372–383.

[9] Carpinteri A, Lacidogna G, Pugno N. Structural damage diagnosis and life-time assessment by acoustic emission monitoring. Eng Fract Mech 2007; 74:273–289.

[10] Giordano F. La Torre Garisenda. Bologna, Italy: Costa; 2000.

[11] Reuters. Bologna's leaning tower to be stabilised by late 2028, mayor says. Reuters 2025 May 13. Available from: https://www.reuters.com/world/europe/bolognas-leaning-tower-be-stabilised-by-late-2028-mayor-says-2025-05-13/

[12] Bologna Today. Torre Garisenda: restauro Bologna 2028 – Matteo Lepore. Bologna Today. Available from:

http://www.bolognatoday.it/cronaca/torre-garisenda-restauro-bologna-2028-matteo-lepore.html

[13] ANSA. Lepore: La torre Garisenda sarà restaurata entro il 2028. ANSA 2025 May 13. Available from: https://www.ansa.it/sito/notizie/cultura/arte/2025/05/13/lepore-la-torre-garisenda-sara-restaurata-entro-il-2028_7659c586-a4ed-462c-8867-ddcd72cca312.html

[14] Lacidogna G, Marin Montanari P, Invernizzi S, Di Tommaso A. The Garisenda Tower in Bologna: Damage assessment results from principal component analysis, acoustic emission, and nonlinear finite element involving creep and smeared cracking. Proc 21st Int Conf Exp Mech (ICEM21), Bologna, Italy; 2025 Jul 6–11. Available from: https://icem-21.org/

[15] Lunitek. Available from: https://www.lunitek.it/ (Accessed 2025 Sep 26).

[16] Friedrich LF, Tanzi BNR, Colpo AB, Sobczyk M, Lacidogna G, Niccolini G, Iturrioz I. Analysis of Acoustic Emission Activity during Progressive Failure in Heterogeneous Materials: Experimental and Numerical Investigation. Appl Sci 2022;12: 3918. https://doi.org/10.3390/app12083918

[17] Gutenberg B, Richter CF. Frequency of earthquakes in California. Bull Seismol Soc Am 1944; 34: 185–188.

[18] Shiotani T, Fujii K, Aoki T, Amou K. Evaluation of progressive failure using AE sources and improved b-value on slope model tests. Prog Acoust Emiss 1994; 529: 534–536.

[19] Carpinteri A, Lacidogna G, Puzzi S. From criticality to final collapse: evolution of the b-value from 1.5 to 1.0. Chaos Soliton Fract 2009;41(2):843–853.

[20] Varotsos PA, Sarlis NV, Skordas ES. Detrended fluctuation analysis of the magnetic and electric field variations that precede rupture. Chaos 2009; 19: 023114.

[21] Gkarlaouni C, Lasocki S, Papadimitriou E, George T. Hurst analysis of seismicity in Corinth rift and Mygdonia graben (Greece). Chaos Solit Fractals 2017; 96: 30–42.

[22] Hurst HE. Long-term storage capacity of reservoirs. Trans Am Soc Civ Eng 1951; 116: 770–808.

[23] Varotsos PA, Sarlis NV, Skordas ES. Study of the temporal correlations in the magnitude time series before major earthquakes in Japan. J Geophys Res Space Phys 2014; 119: 9192–9206.

[24] Skordas ES, Christopoulos SRG, Sarlis NV. Detrended fluctuation analysis of seismicity and order parameter fluctuations before the M7.1 Ridgecrest earthquake. Nat Hazards 2020; 100: 697–711.

[25] Varotsos PA, Sarlis NV, Skordas ES. Spatio-temporal complexity aspects on the interrelation between seismic electric signals and seismicity. Proc Athens Acad 2001; 76: 294–321.

[26] Varotsos PA, Sarlis NV, Skordas ES. Natural Time Analysis: The New View of Time. Berlin: Springer; 2011.

[27] Varotsos PA, Sarlis NV, Skordas ES. Natural Time Analysis: The New View of Time, Part II. Cham: Springer Nature; 2023.

[28] Varotsos PA, Skordas ES, Sarlis NV, Christopoulos SRG. Review of the natural time analysis method and its applications. Mathematics 2024;12(22):3582. https://doi.org/10.3390/math12223582

[29] Hloupis G, Stavrakas I, Vallianatos F, Triantis D. A preliminary study for prefailure indicators in acoustic emissions using wavelets and natural time analysis. Proc Inst Mech Eng L J Mater Des Appl 2016;230(3):780–788.

[30] Niccolini G, Manuello A, Marchis E, Carpinteri A. Signal frequency distribution and natural-time analysis from acoustic emission monitoring of an arched structure in the Castle of Racconigi. Nat Hazards Earth Syst Sci 2017; 10: 1025–1032.

[31] Friedrich LF, Padilha MH, Lacidogna G, Iturrioz I. Multiscale investigation of seismic precursors before major earthquakes. Mech Res Commun. 2025; 147: 104449. https://doi.org/10.1016/j.mechrescom.2025.104449.

[32] Friedrich LF, Cezar ES, Colpo AB, Tanzi BNR, Lacidogna G, Iturrioz I. Identifying impending failure in heterogeneous materials: a study on acoustic emission time series. Chaos Solit Fractals 2024; 185: 115172. https://doi.org/10.1016/j.chaos.2024.115172

[33] Contoyiannis YF, Diakonos FK. Criticality and intermittency in the order parameter space. Phys Lett A 2000;268(4–6):286–292. https://doi.org/10.1016/S0375-9601(00)00203-5

[34] Potirakis SM, Contoyiannis Y, Schekotov A, et al. Evidence of critical dynamics in various electromagnetic precursors. Eur Phys J

Spec Top 2021; 230: 151–177. https://doi.org/10.1140/epjst/e2020-000252-8

[35] Hansen A, Hemmer P, Pradhan S. The Fiber Bundle Model: Modeling Failure in Materials. Statistical Physics of Fracture and Breakdown. Wiley; 2015.

[36] Pradhan S, Hansen A, Hemmer P. Crossover Behavior in Burst Avalanches: Signature of Imminent Failure. Phys Rev Lett 2005; 95: 125501.

[37] Giuffrida A. Bologna seals off ‘leaning tower’ over fears it is tilting too far. The Guardian 2023 Oct 29. Available from: https://www.theguardian.com/world/2023/oct/29/bologna-seals-off-leaning-tower-fears-tilting-too-far

[38] Birck G, Riera JD, Iturrioz I. Numerical DEM simulation of AE in plate fracture and analogy with the frequency of seismic events in SCRs. Eng Fail Anal 2018; 93: 214–223.